J. Fluid Mech. (2003), *vol.* 493, *pp.* 89–119. © 2003 Cambridge University Press
DOI: 10.1017/S0022112003005871 Printed in the United Kingdom

Absolute and convective instability of a relaxational plane liquid jet

By L. DANIEL SÖDERBERG†

Faxén Laboratory and Department of Mechanics, Royal Institute of Technology, SE-100 44, Stockholm, Sweden

(Received 11 August 2000 and in revised form 6 May 2003)

The stability of a plane relaxational liquid jet has been studied theoretically and experimentally through linear stability analysis and flow visualizations. The relaxational liquid jet is obtained by the outflow of a liquid from a plane channel with an upstream fully developed Poiseuille flow into an ambient stagnant gas. Linear spatial stability calculations show that there are five convectively unstable modes, three sinuous and two dilatational. The spatial stability calculations are compared to experimental results for wavenumber variation and the growth of waves found in the visualizations. These variations have been quantified with a wavelet transform and through a comparison with the spatial stability results the type of mode observed in the visualizations has been determined. For this type of mode the calculated wavenumber variation is in good agreement with the experimental results. Also, in the experiments the breakup of the jet has been observed when the Reynolds number reaches a certain value, and as the Reynolds number increases this breakup moves closer to the channel exit. This upstream movement of the breakup can be explained by the linear stability results. Finally the relaxational liquid jet is shown to be absolutely unstable for a certain parameter region. Close to the nozzle both a sinuous mode and a dilatational mode are shown to be absolutely unstable. As the jet profile relaxes to uniform, the sinuous mode is shown to be the only unstable mode. This occurs for Weber numbers $We < 1$, which is in agreement with the theory for liquid jets with uniform velocity profile. The frequency selection for the observed waves is believed to be related to the region of absolute instability located closest to the channel exit.

1. Introduction

Liquid jets were among the first flow phenomena to be investigated within the field of fluid mechanics. The drop formation of a cylindrical liquid jet was studied by Savart (1833) and Plateau (1873), and in the latter half of the 19th century Rayleigh (1896) performed a stability investigation, which made use of linear stability theory. The cylindrical jet is inherently unstable. Since surface tension can be expressed as a surface energy the minimization of the surface area gives an energy minimum. For a liquid cylinder a minimum is obtained if the jet breaks up into pieces $2\pi a$ long that form spherical drops. Here a is the radius of the cylinder.

† Present address: STFI – Swedish Pulp and Paper Research Institute, SE-114 86, Stockholm, Sweden.

https://doi.org/10.1017/S0022112003005871 Published online by Cambridge University Press

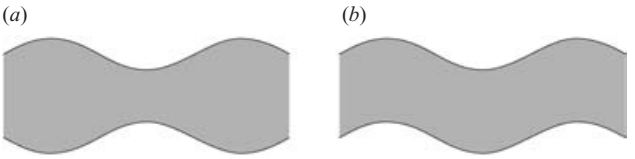


FIGURE 1. Definition of modes, dilatational or varicose (*a*) and sinuous (*b*).

For a planar jet, where the plane perpendicular to the flow direction is basically rectangular with a high width to thickness ratio, the earliest published result was obtained by Squire (1953). This investigation was similar to Rayleigh's of the cylindrical jet. Hence, the streamwise velocity in the jet is assumed to be constant throughout the thickness of the jet, the flow is considered to be inviscid and the presence of an ambient gas is neglected. The surface is subjected to infinitesimal disturbances and the decay or growth of these indicates if the jet is linearly stable or unstable. The result was that the plane jet is stable when subjected to infinitesimal disturbances, which is the opposite to the case with the cylindrical jet. With the assumptions used in this analysis surface tension will always act as a stabilizer, which will force the surface back to its original state, i.e. minimum surface energy.

By assuming that the inviscid jet with uniform velocity profile is surrounded by an inviscid gas Hagerty & Shea (1955) derived a dispersion relation, which indicates that the jet is linearly unstable for a finite wavenumber range. Both dilatational (or varicose) and sinuous disturbances can be unstable, see figure 1. The driving force for this disturbance is the pressure variation on the surface due to the surrounding gas. They also performed experiments on the breakup of the jet.

Later Lin, Lian & Creighton (1990) and Li & Tankin (1991) extended the analysis to include viscosity. This gives two unstable modes similar to the modes identified by Hagerty & Shea (1955). However, Li & Tankin also found a parameter region where viscosity is the driving force for disturbance growth. As an extension to this analysis Lin *et al.* also found the presence of a linear absolute instability of the sinuous mode for low wavenumbers when Weber number $We < 1$.

The spatially developing flow of a plane liquid jet due to the effect of gravity has been studied with respect to local convective and absolute instability by de Luca & Costa (1997). Also, the global instability of this flow was experimentally studied by de Luca (1999). Disregarding the stretching effect of gravity on a vertical liquid jet the basic flow field in a plane liquid jet is normally not uniform but influenced by viscosity, see Tillet (1968). This has a strong effect on the stability, which was investigated with experiments and linear stability theory by Hashimoto & Suzuki (1991). They experimentally showed the presence of fine interfacial waves, which grow downstream. The downstream wavenumber variations found in the visualizations were compared to results from linear stability theory. In order to perform the calculations the basic flow field was obtained with the approximate method presented by Lienhard (1968). These calculations did not include a surrounding gas. The results of the linear stability calculations showed the presence of four unstable modes, two sinuous and two dilatational. Surface tension was neglected in the calculations when the comparison between the experiments and the linear stability was made.

Söderberg & Alfredsson (1998) performed a similar experiment and also solved the two-dimensional Navier–Stokes equations in order to obtain the basic flow field. The calculations included the free surface and the calculated velocity profiles showed good agreement with Pitot-tube measurements. Also, the temporal linear stability of these

https://doi.org/10.1017/S0022112003005871 Published online by Cambridge University Press

velocity profiles was investigated. In these stability calculations the surface tension and the viscous surrounding air were included. The calculations showed the presence of a fifth unstable mode, which is a sinuous mode with no equivalent dilatational mode.

The earlier linear stability results by Hashimoto & Suzuki (1991) and Söderberg & Alfredsson (1998) only show a qualitative agreement with the experimental results. Both investigations are based on the temporal stability formulation; hence the linear wave disturbances grow in time. For this type of experiment where the stability is clearly convective the disturbance frequency is constant throughout the downstream motion of a wave; hence the growth is in space and not in time. Due to this there is an uncertainty in the identification of the mode appearing in the experiments.

The visualizations by Söderberg & Alfredsson (1998) were performed with a thin plane water jet emanating from a channel. At low velocity the jet was perfectly clear and showed no disturbances in either direct or shadowgraph visualizations. Above a certain critical velocity spanwise homogeneous waves appear in the visualizations. When the velocity was increased even more the jet broke up. This breakup occurred along a spanwise homogeneous line, which moved upstream toward the nozzle as the velocity was increased.

The aim with this paper is to gain physical insight in the origin of the waves found in visualizations of the relaxational plane liquid jet. This has been done by a linear spatial stability analysis of the relaxational jet. The results from this analysis are compared to a temporal stability analysis, which is similar to that presented by Söderberg & Alfredsson (1998). The results from the spatial stability analysis are compared to data obtained from visualization images, which were quantified in terms of wavenumber and amplitude variation. The images used are identical to those used by Söderberg & Alfredsson (1998), but are here quantified with the aid of a wavelet transform. Also, the breakdown of the waves is discussed based on the experimental results and the results from the spatial stability calculations. Finally, the possibility of absolute instability of the plane liquid jet is investigated by the contour deformation and cusp-map methods.

2. The linear stability problem

2.1. *Linear stability equations*

The geometry (nozzle and jet) of the flow of a relaxational plane liquid jet can be seen in figure 2. The horizontal x-axis is referred to as the streamwise direction and the vertical y-axis as the normal direction. The velocity fields in the relaxational liquid jet (subscript l) produced by this nozzle and the surrounding gas (subscript g) are divided into basic and disturbance flow fields, which satisfy the governing equations

$$u_{l,g} = \{U_{l,g}(y;X) + u'_{l,g}(x,y,t),\, v'_{l,g}(x,y,t)\}, \tag{2.1a}$$

$$p_{l,g} = P_{l,g}(X) + p'_{l,g}(x,y,t). \tag{2.1b}$$

All variables have been scaled with half the channel thickness, a, and the mean velocity in the channel nozzle, U_m, according to

$$x = x^*/a, \quad y = y^*/a, \quad u = u^*/U_m, \quad v = v^*/U_m, \quad p = p^*/\left(\rho U_m^2\right),$$

where superscript * indicates an unscaled variable and a slow coordinate $X = \epsilon x$, where $\epsilon = 1/Re \ll 1$, has been introduced, which governs the variation of the basic flow. Both the basic flow and the disturbance (denoted by prime) are assumed to be

https://doi.org/10.1017/S0022112003005871 Published online by Cambridge University Press

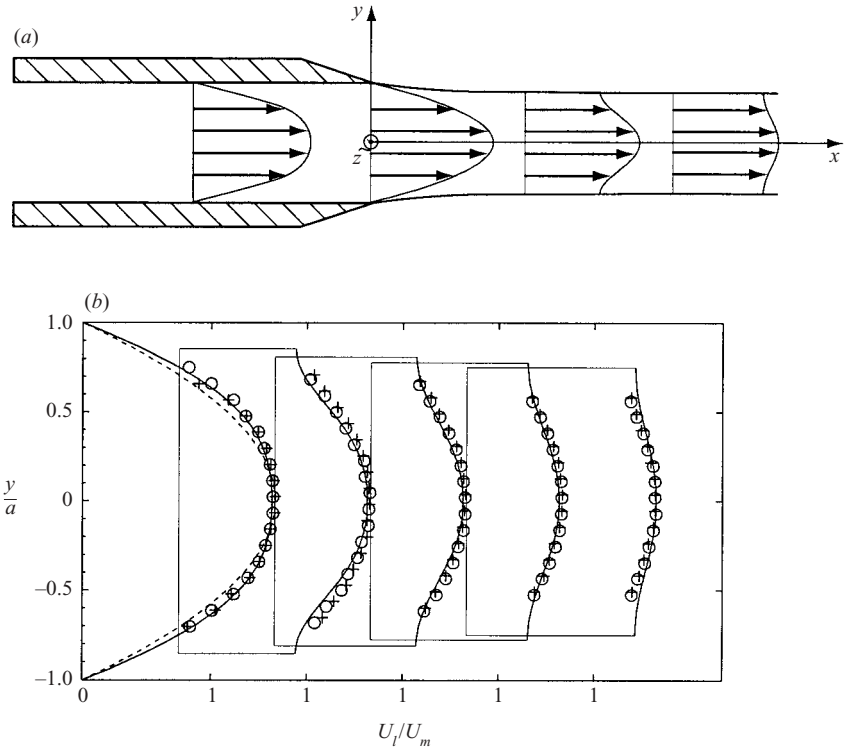


FIGURE 2. (*a*) Channel geometry. (*b*) Velocity distribution in the channel jet. —, calculated; +, ○, measured with pitot-tube; – –, parabolic profile with the same maximum velocity as the measured profile. U_l is the measured/calculated velocity in the liquid (water) and U_m is the mean flow velocity in the channel. $U_m = 1.3\,\mathrm{m\,s^{-1}}$, $a = 0.55\,\mathrm{mm}$, $Re = 700$ and $We = 12.5$, profiles at $x/a = 0$, 18, 36, 55, 73, from Söderberg & Alfredsson (1998).

two-dimensional, i.e. independent of z. The basic flow field of the relaxational liquid jet is taken from the numerical solution by Söderberg & Alfredsson (1998), which is also shown in figure 2 together with Pitot-tube measurements of the streamwise velocity. They found that the flow field was similar when the streamwise coordinate, x, was scaled with the Reynolds number,

$$Re_l = \frac{\rho_l U_m a}{\mu_l}.$$

The similarity gives that $U_l(x/Re, y)$ represents a specific shape of the velocity profile, which was shown to be valid for $Re_l > 100$.

An ansatz is made, where the disturbances are assumed to have the form

$$\{u', v', p'\} = \{\hat{u}(y;X), \hat{v}(y;X), \hat{p}(y;X)\}\mathrm{e}^{\mathrm{i}\Theta(x,t;X)}, \tag{2.2}$$

where the phase $\Theta(x,t;X)$ is given by

$$\Theta(x,t;X) = \int_{x_0}^{x} \alpha(\epsilon\xi)\,\mathrm{d}\xi - \omega t. \tag{2.3}$$

Here α and ω are the wavenumber and frequency respectively. The decomposition (2.1) and the ansatz (2.2) are inserted into the Navier–Stokes equations and linearization is performed. Also, terms containing powers of ϵ, which are a result of the streamwise

https://doi.org/10.1017/S0022112003005871 Published online by Cambridge University Press

variation of the basic flow, are neglected such that the result is the local Orr–Sommerfeld equation,

$$(\mathrm{i}\alpha U - \mathrm{i}\omega)(\mathrm{D}^2 - \alpha^2)\hat{v}_{l,g} - \mathrm{i}\alpha \mathrm{D}^2 U \hat{v}_{l,g} = Re_{l,g}^{-1}(\mathrm{D}^4 - 2\alpha^2\mathrm{D}^2 + \alpha^4)\hat{v}_{l,g}, \tag{2.4a}$$

where $\mathrm{D} = \mathrm{d}/\mathrm{d}y$. This means that the flow locally, i.e. at the position X, is considered to be parallel. The Orr–Sommerfeld equation is formulated with the frequency ω as a parameter instead of the phase velocity, which was used by Söderberg & Alfredsson (1998).

At a specific streamwise position in the liquid jet the free surface is given by $y = \pm\tilde{h}$, where $\tilde{h} = \tilde{h}(X) = h(X)/a$ is the local scaled half-jet-thickness. At the surface four conditions have to be formulated in order to couple the equations (2.4*a*) in the liquid and gas. Also, an equation describing the kinematic condition at the surface has to be added. These conditions are the same as in Söderberg & Alfredsson (1998) and by performing the same procedure as for obtaining the Orr–Sommerfeld equation (2.4*a*) a local linearized formulation of these conditions is obtained,

$$(\mathrm{i}\alpha U_{l,g} - \mathrm{i}\omega)\hat{h}_{\pm\tilde{h}} = \hat{v}_{l,g} \tag{2.4b}$$

$$\hat{v}_l = \hat{v}_g, \tag{2.4c}$$

$$\mathrm{D}\hat{v}_l - \mathrm{i}\alpha\hat{h}_{\pm\tilde{h}}\left(\mathrm{D}U_l - \mathrm{D}U_g\right) = \mathrm{D}\hat{v}_g, \tag{2.4d}$$

$$(\mathrm{D}^2 + \alpha^2)\hat{v}_l - \mathrm{i}\alpha\hat{h}_{\pm\tilde{h}}(\mathrm{D}^2 U_l - \tilde{\mu}\mathrm{D}^2 U_g) = \tilde{\mu}(\mathrm{D}^2 + \alpha^2)\hat{v}_g, \tag{2.4e}$$

$$\begin{aligned}&\left[(\mathrm{i}\alpha U_l - \mathrm{i}\omega) - Re_l^{-1}(\mathrm{D}^2 - 3\alpha^2)\right]\mathrm{D}\hat{v}_l - \mathrm{i}\alpha\mathrm{D}U_l\hat{v}_l \\ &\quad = \left[\tilde{\rho}(\mathrm{i}\alpha U_g - \mathrm{i}\omega) - \tilde{\mu}Re_l^{-1}(\mathrm{D}^2 - 3\alpha^2)\right]\mathrm{D}\hat{v}_g - \mathrm{i}\alpha\tilde{\rho}\mathrm{D}U_g\hat{v}_g - \alpha^4 We^{-1}\hat{h}_{\pm\tilde{h}},\end{aligned} \tag{2.4f}$$

where $\hat{h}_{\pm\tilde{h}}$ are the amplitudes of the disturbance at the two surfaces. The five conditions are derived from the equation for the free surface (2.4*b*), the no-slip condition at the surface (2.4*c*) and (2.4*d*), and finally the normal and tangential stress conditions at the free surface (2.4*e*) and (2.4*f*). Also, Re_g, We, $\tilde{\rho}$ and $\tilde{\mu}$ are the gas Reynolds number, Weber number, density ratio and viscosity ratio, respectively. These are defined as

$$Re_g = \frac{\rho_g U_m a}{\mu_g} \quad We = \frac{\rho U_m^2 a}{\gamma}, \quad \tilde{\rho} = \frac{\rho_g}{\rho_l}, \quad \tilde{\mu} = \frac{\mu_g}{\mu_l}.$$

In order to have a basic flow field in the surrounding gas without making assumptions about the geometry and without having to solve the flow of the gas phase, the solution to Stokes first problem, the infinite starting plate, see e.g. Schlichting (1979), is used,

$$U_g(X, y) = U_l(X, \pm 1)(1 - \mathrm{erf}\,\eta), \qquad \text{where } \eta = (|y| - 1)(Re_g/X)^{0.5}, \tag{2.5}$$

where $U_l(X, \pm 1)$ is the streamwise velocity of the surface of the jet. The time dependence in the solution to Stokes problem has been transformed into a downstream distance with U_m, as done by Söderberg & Alfredsson (1998).

As far-field boundary conditions in the gas the disturbance amplitudes, $\hat{u}$ and $\hat{v}$, are set to zero, which give

$$\hat{v}_g = 0 \quad \text{and} \quad \mathrm{D}\hat{v}_g = 0 \quad \text{at} \quad y = \pm\infty. \tag{2.6}$$

The Orr–Sommerfeld equation and the boundary conditions constitute the eigenvalue problem,

$$\mathscr{D}(\alpha, \omega; Re, We, X)\hat{v}(y) = 0,$$

https://doi.org/10.1017/S0022112003005871 Published online by Cambridge University Press

where $\mathscr{D}$ is a linear differential operator. This gives eigenfunctions $\hat{v}(y)$ only if the parameters satisfy the dispersion relation

$$\mathscr{D}(\alpha, \omega; Re, We, X) = 0. \tag{2.7}$$

The variation of the density and viscosity ratios, $\tilde{\rho}$ and $\tilde{\mu}$, has been omitted, since the problem has been solved only for a water jet in air. Hence, these parameters are constant throughout this investigation.

2.2. *Numerical solution*

The eigenvalue problem has been solved with a spectral method using Chebyshev polynomials. The solution is obtained for the complete system with liquid, gas and the free surface. The solution is represented as,

$$\hat{v} = \sum_{n=0}^{\infty} b_n T_n(y) \quad \text{for} -1 \leqslant y \leqslant 1, \tag{2.8}$$

where T_n is the nth Chebyshev polynomial and b_n are coefficients to be determined. The series is truncated at some finite value of n and inserted into the equation and boundary conditions. This gives a linear system of the form

$$\mathscr{L}\boldsymbol{b} = c\mathscr{M}\boldsymbol{b},$$

where $\boldsymbol{b} = \{b_0, b_1, b_2, \ldots, b_{N+N_{add}}\}$ is the coefficient vector to the Chebyshev expansion (2.8). The matrices $\mathscr{L}$ and $\mathscr{M}$ are given by

$$\mathscr{L} = \mathrm{i}\alpha U(\boldsymbol{T}'' - \alpha^2\boldsymbol{T}) - \mathrm{i}\alpha U''\boldsymbol{T} - \tfrac{1}{Re^{l,g}}(\boldsymbol{T}^{\mathrm{iv}} - 2\alpha^2\boldsymbol{T}'' + \alpha^4\boldsymbol{T}), \tag{2.9}$$

$$\mathscr{M} = \mathrm{i}\alpha(\boldsymbol{T}'' - \alpha^2\boldsymbol{T}), \tag{2.10}$$

where $\boldsymbol{T}^{(k)}$ is a matrix representing the kth derivative of the Chebyshev polynomials. The zeros of the highest-order polynomial are chosen as collocation points, which give

$$y_m = \cos\frac{\pi m}{N}, \quad -1 \leqslant y \leqslant 1, \quad m = 0, 1, \ldots, N + N_{add}.$$

This will give a distribution with grid points clustered at the ends of the interval. The matrices (2.9) and (2.10) have dimension $(N+1)\times(N+1+N_{add})$, where N_{add} depends on how the boundary conditions are treated. These matrices can both be implemented by just adding them to the matrices $\mathscr{L}$ and $\mathscr{M}$ or by substitution of one or two rows at the ends of the numerical domain $-1 \leqslant y \leqslant 1$. All possible combinations were tested and for all results that are presented in this paper the boundary conditions have been implemented both by substitution and by adding them to the matrices.

2.2.1. *Liquid phase*

Because of the extent of the domain (2.8) the equations have locally been re-scaled to local jet thickness and local mean velocity $\widetilde{U} = \widetilde{U}(X)$. It should be noted that the chosen definition of the Reynolds number makes it constant throughout the jet since the quantity $U_m a$ is the mass flow. The Weber number will however change as will the local frequency ω and the wavenumber α if these are fixed globally, table 1.

Because of the symmetry of the basic flow with respect to the centreline of the jet, even and odd solutions to the eigenvalue problem were treated separately (the v- even and odd solutions are equivalent to sinuous and dilatational waves respectively, see figure 1), which meant that the eigenvalue problem could be solved by considering

https://doi.org/10.1017/S0022112003005871 Published online by Cambridge University Press

Variable/parameter	Global	Local	Relation
Reynolds number	$Re_{l,g}$	$\widetilde{Re}_{l,g}$	$\widetilde{Re}_{l,g} = Re_{l,g}$
Weber number	We	$\widetilde{We}$	$\widetilde{We} = We\widetilde{U}^2\tilde{h}$
Coordinate	x	$\tilde{x}$	$\tilde{x} = x\tilde{h}$
Velocity	u	$\tilde{u}$	$\tilde{u} = u\widetilde{U}$
Wavenumber	α	$\tilde{\alpha}$	$\tilde{\alpha} = \alpha/\tilde{h}$
Frequency	ω	$\tilde{\omega}$	$\tilde{\omega} = \omega\tilde{h}/\widetilde{U}$

TABLE 1. Relations between local and global quantities where $\widetilde{U} = \widetilde{U}(X) = U(x)/U_m$ and $\tilde{h} = \tilde{h}(X) = h(x)/a$ are the local dimensionless mean velocity and jet thickness respectively.

only half the jet. Because of this the conditions at the jet centreline do not have to be explicitly set but are given by the choice of symmetry of the Chebyshev polynomial in the liquid phase.

2.2.2. *Gas phase*

In the gas phase the numerical domain of the Chebyshev polynomial, $-1 \leqslant y \leqslant 1$, was re-scaled to the domain $1 \leqslant y \leqslant y_f$, where y_f is the position of the outer boundary. This made it possible to move the free-boundary condition away from the surface. The boundary conditions (2.6) were then imposed at this point, which made it possible to study of the effect of the location of the free-stream boundary condition. Two different positions were tested, $y_f = 1 + 6\,\delta_{99}$ and $y_f = 1 + 12\,\delta_{99}$, where δ_{99} is the thickness of the boundary layer in the gas. These choices gave the same result for all unstable modes and hence the effect of a finite domain should not have an effect on the results that are presented.

2.2.3. *Solution of the eigenvalue problem*

The eigenvalue problem was solved both for temporal modes ($\alpha \in \boldsymbol{R}$) and spatial modes ($\omega \in \boldsymbol{R}$). Also, the general problem was considered where both α and ω are complex. The numerical problem was solved by the generalized eigenvalue solver, *eig*, built into the commercially available mathematical software *Matlab* version 5.2.

The linear stability problem contains several parameters, i.e. Re, We, $\tilde{\mu}$ and $\tilde{\rho}$, and it is also a function of the downstream position in the jet. The results presented here are based on the flow of a water jet into air. This means that $\tilde{\mu}$ and $\tilde{\rho}$ will be kept constant. For $T = 20^{\circ}\mathrm{C}$ the viscosity for water is $\mu_l = 1.01 \times 10^{-3}\,\mathrm{kg\,m^{-1}\,s^{-1}}$ and for air $\mu_g = 1.79 \times 10^{-5}\,\mathrm{kg\,m^{-1}\,s^{-1}}$, which gives a viscosity ratio $\tilde{\mu} = 0.0177$. Similarly for the density $\rho_l = 997\,\mathrm{kg\,m^{-3}}$ and $\rho_g = 1.21\,\mathrm{kg\,m^{-3}}$, which gives $\tilde{\rho} = 1.21 \times 10^{-3}$. The surface tension was set to $\gamma = 0.070\,\mathrm{N\,m^{-1}}$.

In order to check the accuracy of the solution several tests were made. These consisted of grid refinement as well as a variation of the extent of the physical domain. In figure 3 the effect of resolution can be seen. In the figure both spatial and temporal results are shown. The most unstable modes seem to be well-converged. It should be noted that for $N = 90$ the temporal solution gives matrices that are 180×180 and the spatial solution 720×720. Thus the numerical solution to the spatial problem is much more time consuming. The linear stability problem encountered gives rise to five possible unstable modes, three sinuous and two dilatational. This was shown by Söderberg & Alfredsson (1998), who solved the temporal stability problem. These five modes can be seen in figure 4, which is a magnification of the results in figure 3. Figure 4(*a*) represents temporal modes and figure 4(*b*) spatial modes. The sinuous

https://doi.org/10.1017/S0022112003005871 Published online by Cambridge University Press

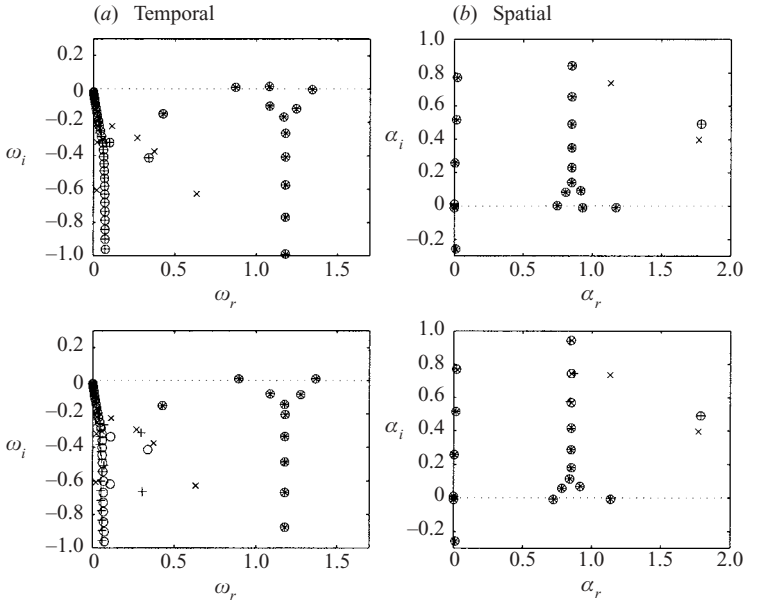


FIGURE 3. Eigenvalue spectra and numerical accuracy, $Re = 1000$, $We = 25.5$ and $x/Re = 0.07$. With sinuous (even) modes shown in the top plots and dilatational (odd) in the bottom. In the temporal formulation $\alpha = 1$ and in the spatial $\omega = 1$. $\times$, $N_l = N_g = 30$; $\circ$, $N_l = N_g = 60$; $+$, $N_l = N_g = 90$.

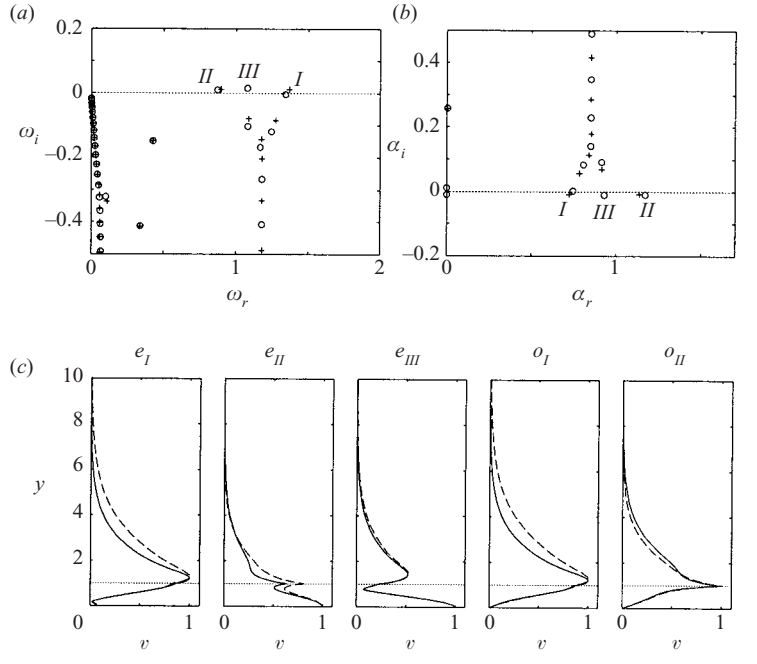


FIGURE 4. (a, b) Eigenvalue spectra and (c) eigenfunctions, $Re = 1000$, $We = 25.5$ and $x/Re = 0.07$. In temporal formulation $\alpha = 1$ and in spatial $\omega = 1$. For the v-eigenfunctions, (c), temporal eigenfunctions (solid) and spatial eigenfunctions (dashed are shown). The classification of the type is also shown (I, II and III).

https://doi.org/10.1017/S0022112003005871 Published online by Cambridge University Press

(even) modes are denoted e_I, e_{II} and e_{III} and the dilatational (odd) modes are denoted o_I and o_{II}. Here I, II and III represents their 'type', which also is indicated in the figure.

In these spectra four of the modes are unstable and the fifth is a sinuous mode which is almost unstable, e_I, to the right (left) in the temporal (spatial) graph. For the set of parameters used here there are never five simultaneously unstable modes. In figure 4(c) the eigenfunctions for these modes can be seen in both liquid and gas. The graphs show the results both for the temporal formulation as well as the spatial formulation. As can be seen all eigenfunctions decay far away from the free surface.

2.2.4. *Identification of absolute instability*

The flow of the plane liquid jet was also investigated with respect to a possible absolute instability, since this has been observed for the uniform plane liquid jet, see Lin *et al.* (1990). The flow is spatially varying and the analysis was performed for local velocity profiles. Both the contour deformation and the cusp-map methods have been applied, see e.g. Huerre & Monkewitz (1990). The contour deformation method makes it easy to identify α^+ and α^- branches (following the notation of Huerre & Monkewitz 1990).

In figure 5 an example of a pinch point, (α_0, ω_0), for the dilatational (odd) mode of type II is shown. In figure 5(a) the complex α-plane is shown where branch-cuts have been introduced at the imaginary axis and the grey region indicates stable α^+ modes, i.e. $\alpha_i^+ > 0$. In figure 5(b) the corresponding ω-plane can be seen.

Initially the integration contour Ω in the complex ω-plane is located above the real axis. The integration contour is a horizontal line with fixed ω_i where ω_r takes all real values. When the contour is lowered toward the real axis a pinch point is formed by the two branches o_{II}^+ and o_{II}^-. For higher values of ω_i it can be clearly seen that o_{II}^+ and o_{II}^- originate in the upper and lower half-plane respectively. Also, the o_I^+ mode can be seen in this graph. This is also a + mode, which originates in the upper half-plane.

The dashed curves in the α-plane represent the traces of the different modes when the integration contour in the ω-plane is slightly higher than $\omega_{0,i}$. In (b) the integration contour Ω (thick dotted line) in the ω-plane corresponds to the pinching of the o_{II}^+ and o_{II}^- branches. When this contour is followed it gives rise to the solid curves in the α-plane. The integration contour F (thick dotted curve) in the α-plane is shown, which passes through the pinch point. When this integration contour F is followed it gives rise to the curves in the ω-plane, which are the traces of the different modes. In the ω-plane two curves are labelled, corresponding to o_I and o_{II}. As can be seen the o_{II}-curve shows a cusp at pinching (ω_0).

All modes ($e_{I,II,III}$ and $o_{I,II}$) shown in figure 4 have been verified to be + modes, i.e. modes that originate in the $\alpha_i > 0$ plane for higher values of ω_i.

Due to the complexity of the problem with several modes present, the pinch-points have to be located manually. For each velocity profile the Reynolds number that gave $\omega_{0,i} = 0$ was identified and the result was checked with grid refinement. This is tedious and time consuming. Hence, only the curve $\omega_{0,i}(x/Re, Re) = 0$ was solved and not the complete function $\omega_{0,i}(x/Re, Re)$. Because of this the 'fine structure' of the absolute instability has not been investigated, i.e. the flow has not been investigated with respect to global stability or instability, see e.g. Huerre & Monkewitz (1990, pp. 490–499).

https://doi.org/10.1017/S0022112003005871 Published online by Cambridge University Press

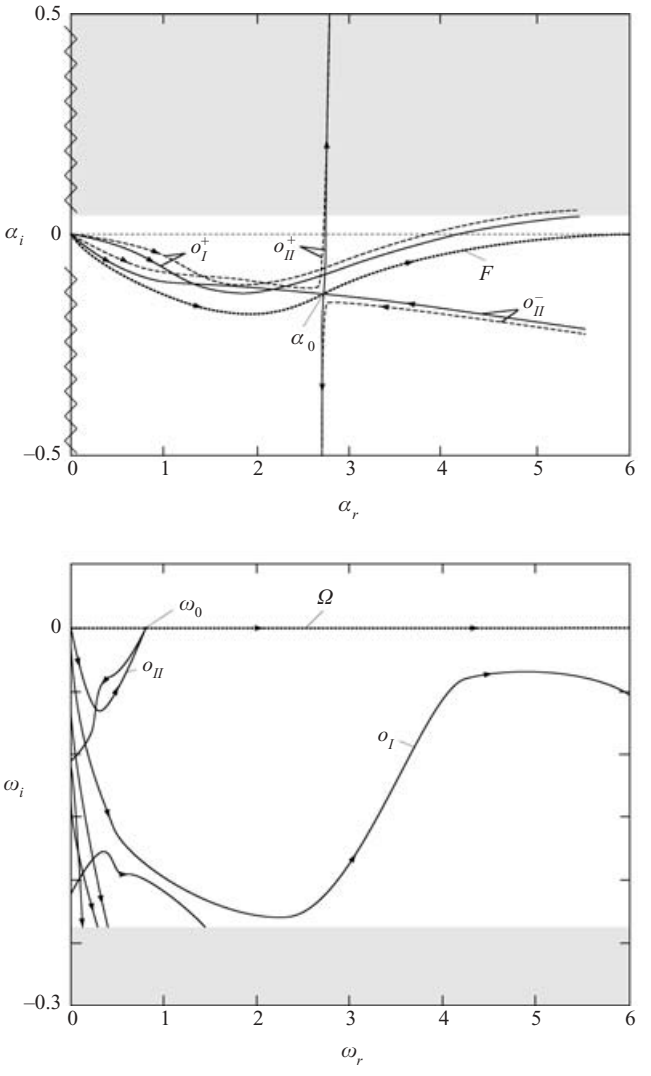


FIGURE 5. Pinching of the dilatational (odd) mode of type *II*, $Re = 797$, $We = 13.7$, $x/Re = 0.010$, $\alpha_0 = 2.73 - 0.13i$ and $\omega_0 = 0.81$. (*a*) The complex α-plane at pinching (solid lines). (*b*) The corresponding complex ω-plane. A detailed description of these graphs are found in § 2.2.4.

3. Experimental set-up

3.1. *Flow apparatus*

The experiments were performed using the set-up depicted in figure 6, which is the same as in Söderberg & Alfredsson (1998). In the figure the apparatus, which was used to produce the plane water jet, can be seen from two different angles. At the bottom of this 'headbox' the plane channel was mounted. The jet from the channel is directed vertically into a dump-tank in which a centrifugal pump is submerged. The water is fed from the pump to the headbox through a hardened PVC hose, which is connected to a stiff PVC tube just upstream of the headbox. The PVC tube was divided into two before entering the headbox. The flow rate was adjusted

https://doi.org/10.1017/S0022112003005871 Published online by Cambridge University Press

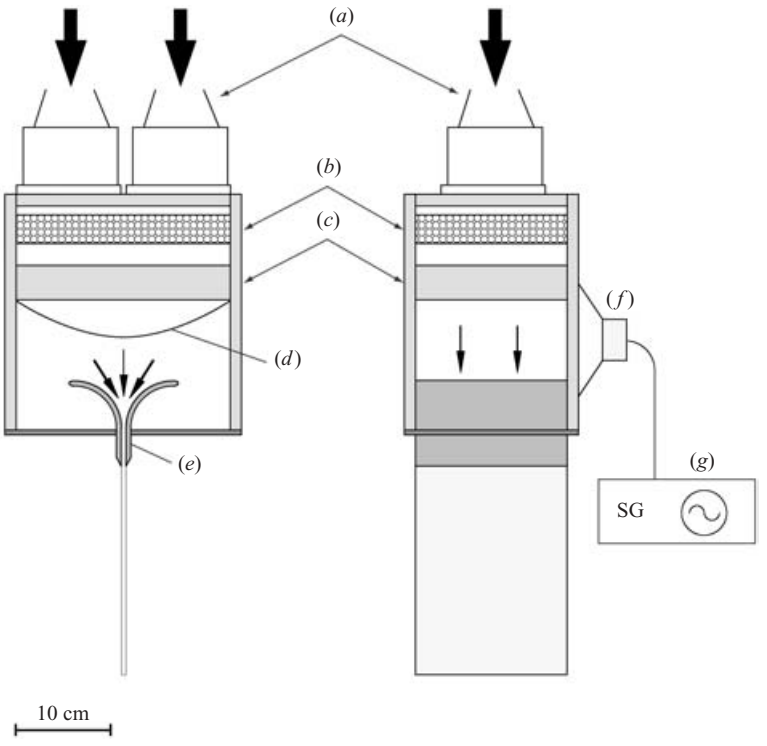


FIGURE 6. Experimental set-up. (*a*) Centrifugal pump, (*b*) glass beads, (*c*) honeycomb, (*d*) screen, (*e*) plane channel, (*f*) speaker and (*g*) signal generator.

with a valve downstream of the pump. With the 1.1 mm channel width used in the experiments ($a = 0.55$ mm) it was possible to obtain a jet velocity (U_m) of 13 m s^{-1}. This corresponds to a maximum Reynolds number of about 7×10^3.

The headbox has the dimensions $25 \times 25 \times 15$ cm^3 and was made of Plexiglas allowing optical access to its interior. The spanwise width of the nozzle (channel) was 15 cm. In order to reduce disturbances the water, when entering the headbox, passed through a flow distributor consisting of a 30 mm thick bed of packed 4 mm diameter glass beads. Downstream of this distributor the flow passed through two fine meshed screens that reduce the turbulence level and also give a pressure drop which improves the uniformity of the flow.

Downstream of the screens a 6 cm long honeycomb with a cell diameter of 5 mm aligns the flow. Finally an arc-shaped screen was mounted with the top directed in the flow direction. This made it possible for air bubbles to move up to the sides at start up of the flow loop. Air bubbles became easily stuck to this screen and therefore it was possible to manually vibrate the screen by inserting a bar from the nozzle opening. This last screen had a porosity of 0.60 and for all velocities the Reynolds number based on wire diameter was less than 10, hence this final screen was sub-critical with respect to vortex shedding. A pressure transducer was mounted on the wall of the headbox downstream of the last screen and the transducer output was calibrated against the jet flow rate.

The channel nozzle consisted of a contraction made of two quarter-cylinders with a radius of 5 cm followed by two 4 cm long flat plates, all made of brass. Before any experiments were performed the nozzle was carefully polished and the sharp edges

https://doi.org/10.1017/S0022112003005871 Published online by Cambridge University Press

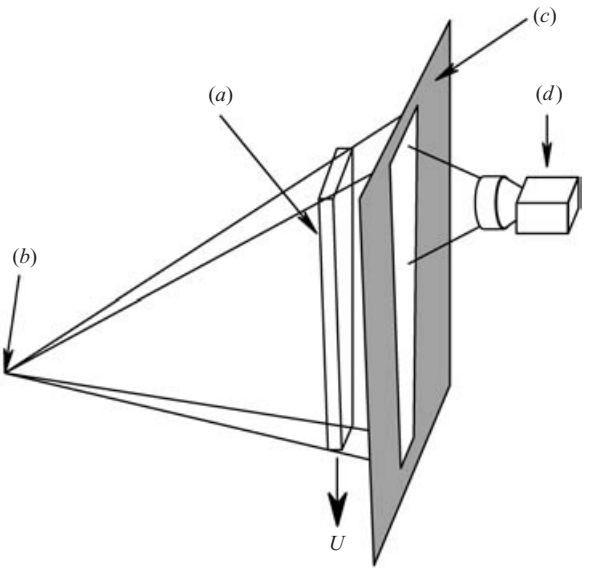


FIGURE 7. Principle of shadowgraph visualization: (*a*) liquid jet, (*b*) light source, (*c*) semi-transparent plate and (*d*) camera.

were checked regularly to ensure that they had no damage that could disturb the jet. Damage to the edges (or even a water droplet stuck at the outlet) showed in the visualizations as a stationary wave pattern on the surface having a Λ-shape with the origin at the edge.

In order to trigger wave disturbances a loudspeaker was firmly attached to the headbox. This position of the speaker can also be seen in figure 6. It was driven by a signal generator, which allowed control of the amplitude and frequency of a sinuous signal.

3.2. *Visualization method*

The flow of the jet was visualized by the shadowgraph method, figure 7, implemented by placing a slide projector far away from the jet, in order to simulate a point light source. The light (rays) from the projector are almost parallel when they reach the jet. As the light passes through the jet the curvature of the surface will cause refraction of the rays. When the rays reach the semi-transparent plate a pattern will appear, i.e. shadows.

3.3. *Quantification of images by wavelet transform*

Quantitative data from the visualization images were obtained using a continuous wavelet transform, see e.g. Farge (1992). The images captured with the CCD camera were transferred to a computer and the surface variations were obtained from a relation between light intensity and surface curvature.

The surface variations were quantified with a Morlet continuous wavelet transform, which makes it possible to obtain both the spatial variation of the wavenumber and the amplitude. The Morlet wavelet consists of a sinuous function weighted by a Gaussian function. From a time series of 100 images a vertical line of pixels was extracted from the centre of each image. The Morlet wavelet was applied on these signals, after which averaging was performed.

https://doi.org/10.1017/S0022112003005871 Published online by Cambridge University Press

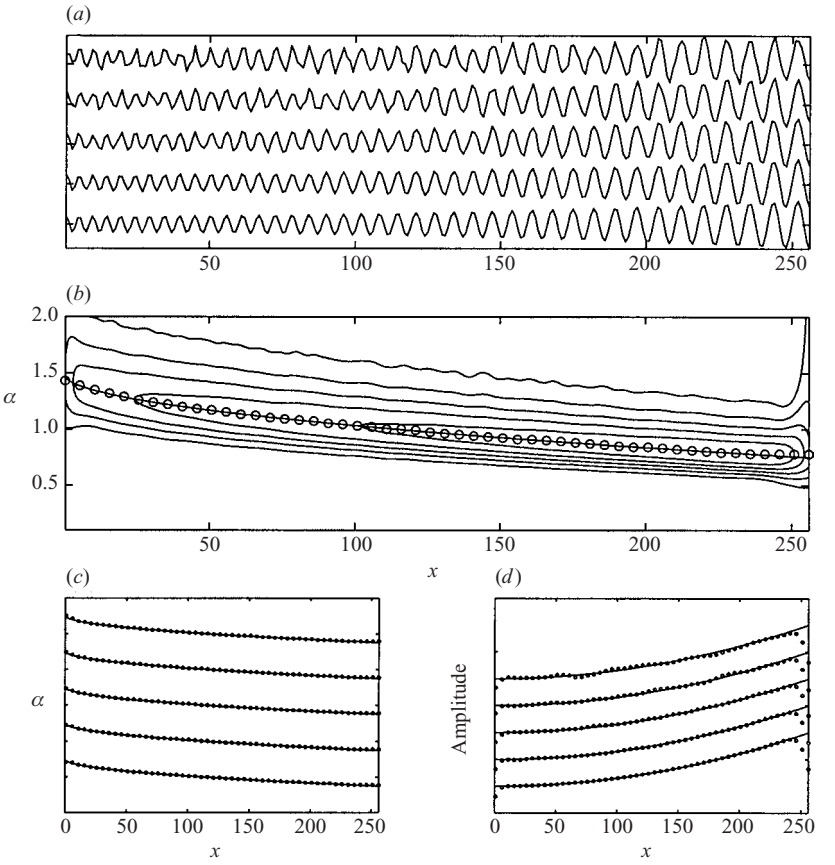


FIGURE 8. Example of signal generated analysed with the wavelet method. (*a*) Example of signals generated. (*b*) Contour plot of wavelet amplitude map, $G = 0.3$: ○, detected wavenumber variation; —, exact. (*c*) Wavenumber variation and (*d*) amplitude variation. In (*a*), (*c*) and (*d*) from bottom to top $G = 0$, 0.3, 0.6, 0.9, 1.2. In (*c*) and (*d*), ●, detected variation and —, exact.

In order to test and validate the method 100 images (signals) with known wavenumber and amplitude variation were created. These had the form

$$I(x) = A(x)\sin\theta(x) + Gr(x),$$

where $I(x)$ is the intensity, $A(x) \in [0, 2]$ the amplitude variation, $\theta(x)$ the phase, $r(x) \in [0, 1]$ a random uniform noise and G the noise level. The wavenumber is obtained from

$$\alpha(x) = \frac{\mathrm{d}\theta}{\mathrm{d}x}.$$

In figure 8 the results of this test are presented for a wavenumber and image resolution which is representative for the experiments performed. Figure 8(*a*) shows examples of the signals generated. From top to bottom, the noise level decreases. Also, the wavelength is slowly increasing in the x-direction as is the amplitude. The resulting wavelet map in figure 8(*b*) is the result of averaging over 100 generated signals. In this figure the wavelet map is shown as a contour plot. The maximum ridge can be clearly seen. At each x-position the maximum of the wavelet transform is extracted along the vertical wavenumber axis, and is represented with circles. This gives both

https://doi.org/10.1017/S0022112003005871 Published online by Cambridge University Press

a dominant wavenumber and its related amplitude. In the figure the exact (known) variation is also plotted as a solid line.

The sensitivity to disturbances is shown in figure 8(*c*, *d*) as the extracted wavenumber and amplitude variations for the noise levels shown in (*a*). As can be seen, the wavelet method is rather insensitive to random noise. However, deterministic noise with a spatial periodicity can degrade the result severely.

3.4. *Relation between light intensity and surface amplitude on the jet*

Since the velocity profile in the jet is varying, it is difficult to measure the growth rate without measuring the whole jet profile, both for u and v. However, the amplitude of the surface is accessible if the variations in greyscale due to the waves in the jet can be related to the surface amplitude. Based on geometrical optics, with the assumption of central rays, a thin sheet thickness $2h$ and small amplitude (relative to the sheet thickness) an expression can be deduced that gives the amplitude h' of the free surface,

$$h'(x) = \frac{1}{2\sigma h(x)\alpha_r(x)^2}\left|\frac{\Lambda(x)}{1-\Lambda(x)^2}\right|, \tag{3.1}$$

where $\Lambda(x)$ is the maximum variation in light intensity relative to the mean intensity at a fixed streamwise position and $\sigma = d(n_g/n_l - 1)$, where $n_{l,g}$ are the indexes of refraction for the liquid and gas respectively and d is the distance between the jet surface and the shadowgraph image. This expression is monotonic, which is not correct for larger amplitudes and longer distances d.

The results obtained for surface amplitude variation should be treated with caution for two reasons. First, the method used to obtain the surface amplitude from intensity variations is only valid for small amplitudes (depending on wavenumber), found by simulating the shadowgraph method numerically. Such simulations were performed for the parameters used in the experiment and the agreement was good for $h' < 0.1h$. Second, linear stability results are based on the assumption of infinitesimal disturbances, which seems to be violated since the waves that appear on the surface of the jet can be seen with the naked eye.

4. Results

The results in this section are based on the flow of a plane water jet in air and the parameters used can be found in § 2.2.3. These parameters are the same as those used in Söderberg & Alfredsson (1998).

4.1. *Spatial stability*

By tracking the downstream movement of the individual modes for variations of α or ω, it is possible to obtain contour plots such as in figures 9 and 10. These two figures show the unstable regions (grey-shaded), for all five modes at $Re = 1000$, and from the temporal (left column) and the spatial (right column) formulations. In figure 9 the three unstable sinuous modes are shown, from top to bottom, denoted e_I, e_{II} and e_{III}, as in figure 4. The horizontal axis is the streamwise position scaled with the Reynolds number. Because of the similarity of the flow field a fixed x/Re implies a fixed velocity profile. This axis is the same for both the temporal and the spatial results. The vertical axis represent a real wavenumber α for the temporal formulation and a real angular frequency ω for the spatial formulation. In the graphs the temporal and spatial growth rates are shown as contour levels, which represent constant values of ω_i and $-\alpha_i$, respectively. Also, ω_r (α_r) is shown by dashed lines in the temporal

https://doi.org/10.1017/S0022112003005871 Published online by Cambridge University Press

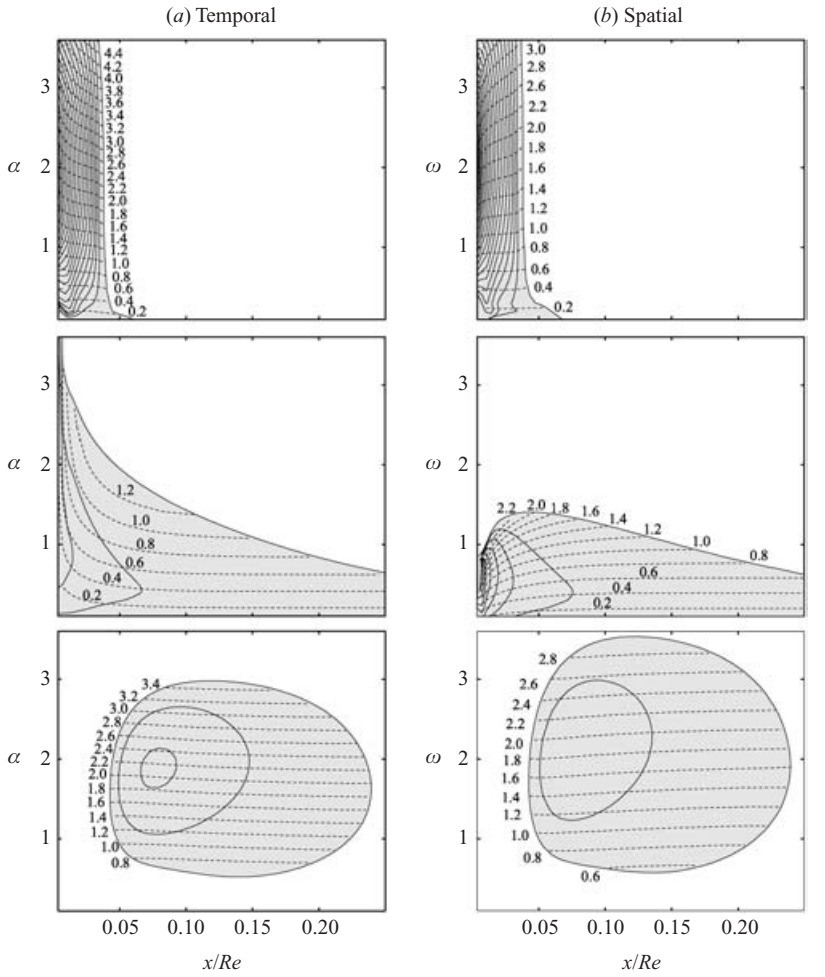


FIGURE 9. Contour plots representing sinuous unstable modes. (*a*) Temporal formulation, where the solid contours represent constant values of ω_i ($\Delta\omega_i = 0.02$) and the labelled dashed contours represent constant values of ω_r. (*b*) Spatial formulation, where solid contours represent $-\alpha_i$ ($\Delta\alpha_i = 0.02$) and the labelled dashed contours represent constant values of α_r. $Re = 1000$ and $We = 25.5$. From top to bottom, modes of type *I*, *II* and *III*.

(spatial) graph. The linear stability has only been solved in the region $\alpha \in [0.1, 3.6]$ ($\omega \in [0.1, 3.6]$) for temporal (spatial) stability. The first streamwise position is at $x/Re = 0.0037$, which for $Re = 1000$ gives $x = 3.7$.

For the first mode, *I*, the temporal and spatial results give similar graphs. Maximum growth rate for the temporal case is $\omega_i = 0.38$, which corresponds to $\alpha = 1.96$ and $\omega_r = 2.04$. Maximum growth rate for the spatial case is $-\alpha_i = 0.40$ corresponding to $\omega = 2.10$ and $\alpha_r = 2.01$. Hence, the maximum is not identical in the two different formulations. Maximum spatial growth is obtained for a slightly higher wavenumber and higher frequency compared to the maximum temporal growth. It should also be noted that the neutral curves are almost straight lines, which are parallel to the vertical axis. For the second mode, *II*, the temporal and spatial results are different. For the temporal formulation, close to the nozzle the unstable region covers all wavenumbers. Downstream of this region it shifts towards lower wavenumbers. The

https://doi.org/10.1017/S0022112003005871 Published online by Cambridge University Press

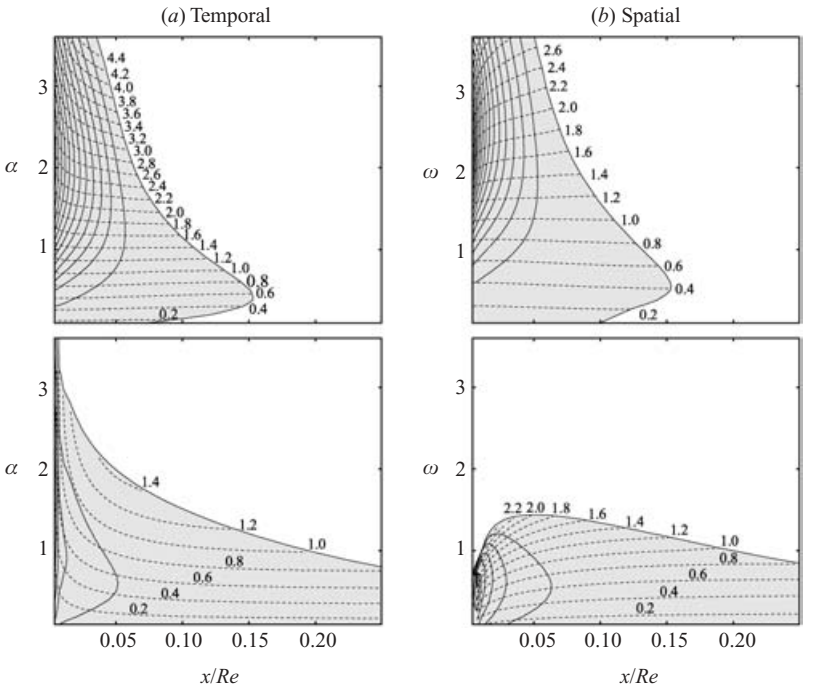


FIGURE 10. Contour plots representing dilatational unstable modes, I (top) and II (bottom) for (a) temporal and (b) spatial formulation. For description see figure 9.

spatial formulation gives the result that the mode is unstable for low frequencies. The third mode, III, which only can be found for sinuous disturbances, is unstable in a bounded parameter region given by $\alpha_r \approx 0.6$–3.0, $\omega_r \approx 0.6$–3.4 and $x/Re \approx 0.05$–0.24.

The dilatational modes, denoted o_I and o_{II} in figure 10, behave qualitatively in the same way as the sinuous modes of the same type. However, they have a slightly different unstable region, which can be seen in figure 11, where the boundaries of the unstable domains are plotted. From this graph it is also clear that there is no point in the (α, x/Re)-plane where all five modes are simultaneously unstable.

Also, in figure 11 examples of the eigenfunctions associated with the modes are plotted for $\alpha = 1$ and $x/Re = 0.07$. At this position the velocity profile is very similar to the profile at $x/a = 55$ ($x/Re = 0.078$) shown in figure 2 and the eigenfunctions are the same as in figure 4 but here presented for the liquid jet only. The eigenfunctions show the amplitude distribution $\hat{u}$ and $\hat{v}$, with the $y/\tilde{h}$-coordinate on the vertical axis. The modes of type I are seen to have a maximum in $\hat{u}$ close to the inflection point in the profile, which is located at $y/\tilde{h} \approx 0.5$, see Söderberg & Alfredsson (1998). Also, for this type the $\hat{v}$ amplitude is maximal at the surface for both modes.

From figure 11 it appears that the modes of type II have their maximum amplitudes at the surface (for the case of e_{II} the amplitude at the centreline is slightly higher). This could be a sign that the effect of surface tension is more important for this type. Finally, the type III mode seems to be coupled to the velocity profile in the liquid jet with low amplitudes at the surface.

4.2. *Fixed-frequency forcing*

In the experiments presented in Söderberg & Alfredsson (1998) there are no signs of disturbances at low jet velocity except capillary waves originating from the side

https://doi.org/10.1017/S0022112003005871 Published online by Cambridge University Press

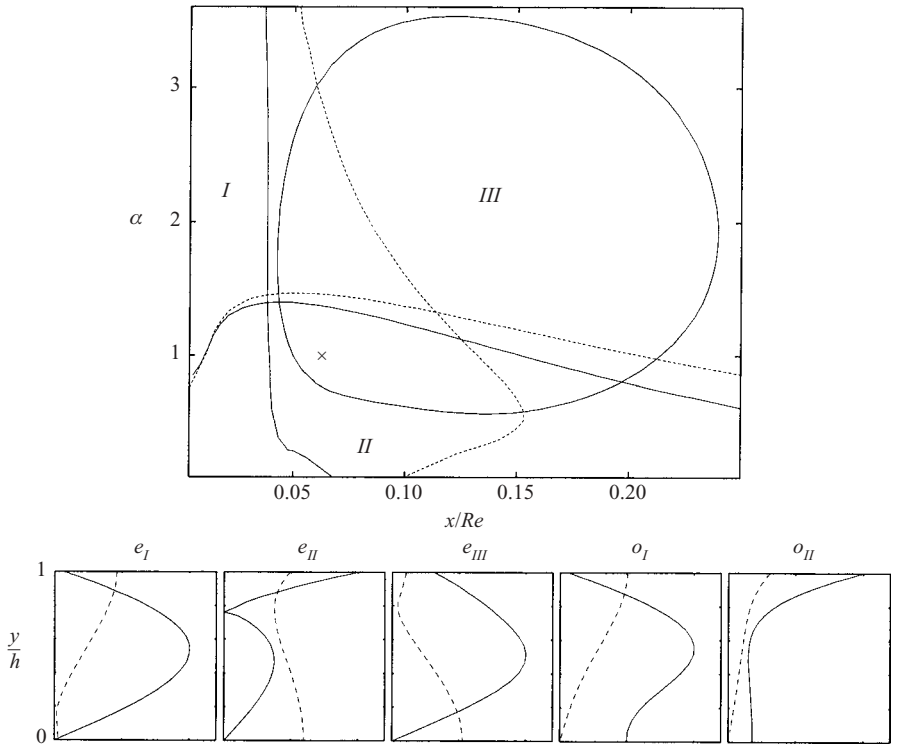


FIGURE 11. (*a*) Location of sinuous (—) and dilatational (- - -) unstable modes at $Re = 1000$ and $We = 25.5$ and (*b*) eigenfunctions for all three types of modes. Modes are shown for $\alpha = 1$ and $x/Re = 0.07$ (marked by $\times$ in (*a*)). In (*b*) —, $|\hat{u}|$ and - - -, $|\hat{v}|$.

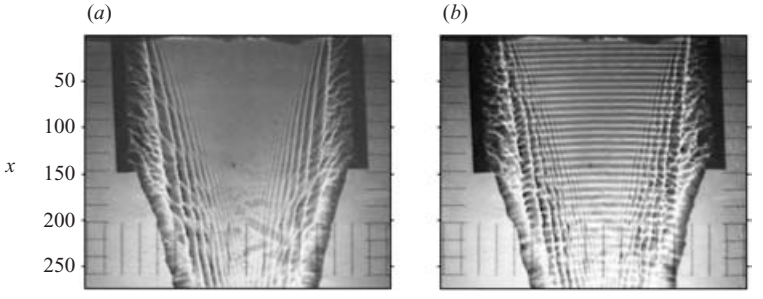


FIGURE 12. Shadowgraph visualization of plane jet at $Re = 700$, $We = 12.5$ and $a = 0.55$ mm. (*a*) Undisturbed and (*b*) with acoustic forcing, $f = 669\,Hz$. The images are taken from Söderberg & Alfredsson (1998).

bars, see figure 12(*a*). In this image the jet is flowing from top to bottom and the spatial extent can be identified by the centimetre markings on the opaque plate. If, however, the speaker is turned on, a spanwise homogeneous pattern can be observed in the shadowgraph visualization, figure 12(*b*). This pattern is a result of waves on the surface of the jet and when the acoustic forcing is removed the waves disappear, which is typical behaviour of convective modes that propagate in space.

In order to compare the wavenumber and amplitude variation obtained in the experiments with linear stability results, a spatial formulation was used where a real

https://doi.org/10.1017/S0022112003005871 Published online by Cambridge University Press

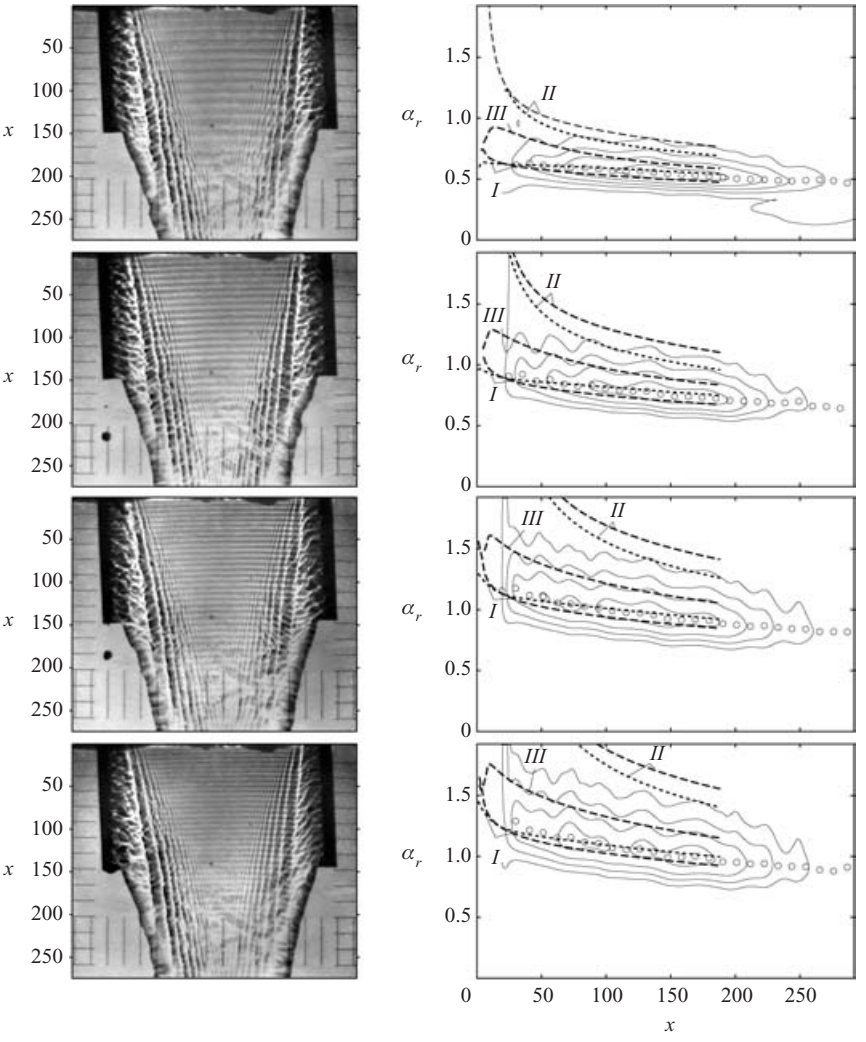


FIGURE 13. Comparison between experimental and theoretical results on wavenumber variation, from top to bottom $f = 340$, 485, 612, 669 Hz. $Re = 700$, $We = 12.5$ and $a = 0.55$ mm. (*a*) Sample images with forced wave disturbances and (*b*) results from wavelet transform and theory. In the contour plots the experimental maximum is marked ○ and wavenumber variation from spatial stability theory is shown both for sinuous (— — —) and dilatational (· · ·) modes. The type of mode is indicated on the graphs (*I,II,III*). The images are taken from Söderberg & Alfredsson (1998).

frequency can be fixed, $\omega \in \boldsymbol{R}$. The wavenumber is then obtained as $\mathrm{Re}\{\alpha^+\} = \alpha_r$, and the growth rate as $-\mathrm{Im}\{\alpha^+\} = -\alpha_i$. Here α^+ is the downstream response to the forcing, which was checked by the contour deformation method as described in § 2.2.4. In order to make a comparison with the experimental results the basic flow field in the stability calculations, $Re = 700$ with the presence of gravity, was taken from Söderberg & Alfredsson (1998), see figure 2.

Figure 13 shows a comparison between the experimental and theoretical results. The jet was forced at four different frequencies, which yield images similar to figure 12(*b*). By the wavelet method described in § 3.3 the wavenumber variation was extracted

https://doi.org/10.1017/S0022112003005871 Published online by Cambridge University Press

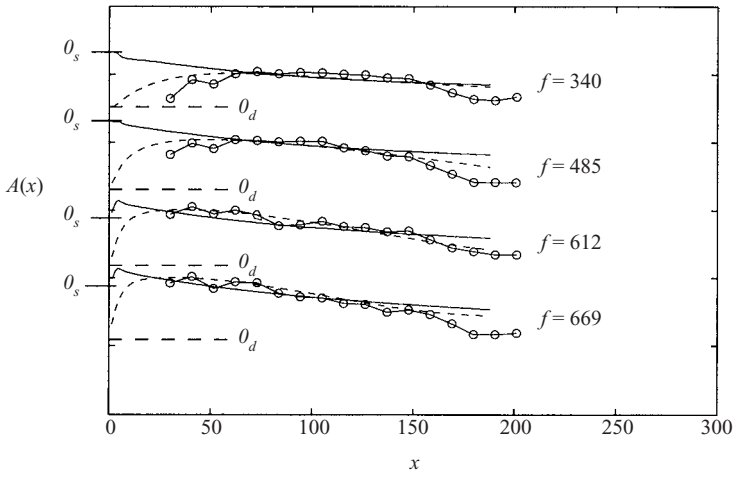


FIGURE 14. Measured amplitude and integrated growth as a function of downstream position for modes of type *I*: —, sinuous mode, - - - -; dilatational mode, ○; measured amplitude. $Re = 700$, $We = 12.5$ and $a = 0.55$ mm.

as a function of downstream position. In figure 13(*b*) four graphs are shown, which represent the four forcing frequencies. In each graph the wavenumber is plotted as a function of the non-dimensional x-coordinate. The wavenumber variation for the three sinuous and two dilatational modes is plotted on top of the wavelet transform map, *cf.* figure 8(*b*). It is possible to conclude from these graphs that the observed waves initiated by acoustic forcing probably are of type *I*. For the four frequencies the wavenumber is decreasing downstream in the jet. Also, a higher frequency gives a higher wavenumber. The modes of type *I* have the lowest wavenumber, which is roughly one-half that for the modes of type *II*. In between these two pairs of modes the fifth (sinuous) unstable mode is found.

By making use of the relation between the wave amplitude and the variation of light intensity in the images, (3.1), it is possible to obtain an estimate of the downstream amplitude variation of the waves, see figure 14. In this figure the logarithm of the measured amplitude variation is plotted as well as the integrated growth $A(x)$ from the stability calculations, which is defined as

$$A(x) = \int_0^x -\alpha_i(\epsilon\xi)\,\mathrm{d}\xi.$$

Since the initial amplitude of the disturbance is unknown a constant has to be added. This constant has been fitted where the measured amplitude obtains a maximum. The validity of the experimental method is discussed in § 3.4. However, from the figure it appears that the waves in the images could correspond to the dilatational mode, mainly since the sinuous mode appears to grow only very close to the nozzle and for the two lowest frequencies the calculations do not give any growth at all. For both dilatational and sinuous modes the zero-level for the calculated growth is indicated in the graph by 0_d and 0_s respectively. The results seem to be in agreement with the visual appearance of the images, where the contrast clearly decreases in the downstream direction. Hence there seems to be a qualitative agreement between the experimental and theoretical results.

https://doi.org/10.1017/S0022112003005871 Published online by Cambridge University Press

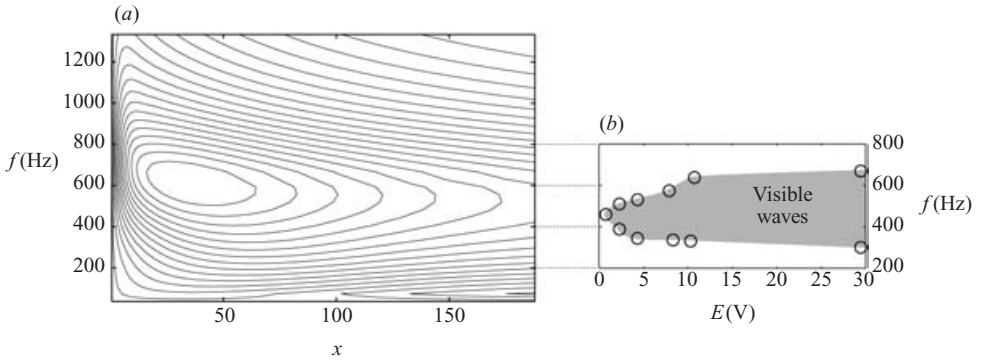


FIGURE 15. (*a*) Integrated growth rate for dilatational mode of type *I* at $Re = 700$ and (*b*) bounds from changing frequency and forcing amplitude.

In figure 15(*a*) the integrated growth rate is plotted as a contour plot. The vertical axis is unscaled and the horizontal axis represents the downstream position scaled with the half-channel thickness. The contour levels represent lines of constant integrated growth rate. As can be seen, there is a maximum at $x \approx 40$ and $f_{max} \approx 600$ Hz. Further downstream the ridge of maximum growth shifts to slightly lower frequencies, which means that the maximum amplitude will occur at slightly different positions depending on the frequency. After the maximum point the amplitude will decay. This behaviour is a result of the streamwise variation of the basic flow. Also, for these flow conditions and parameters the integrated growth of the sinuous mode is lower than for the dilatational mode.

Experimentally the maximum amplification was sought by altering the power (voltage), *E*, and frequency to the speaker. Without forcing the visualizations show no signs of waves, as in figure 12(*a*). In order to obtain visible waves, the speaker has to be turned on and the lowest voltage needed to see waves was found to be 540 Hz. The voltage supply to the speaker was then altered and the frequencies that gave visible waves were recorded. This result can be seen in figure 15(*b*). The response of the speaker has not been considered and the interpretation may not be straightforward, but it gives a qualitative agreement with the integrated growth rate.

4.3. *Integrated growth*

The previous section shows a comparison between experiments and theory regarding growth rate and wavenumber variation. Based on this it appears that the mode present in the jet is dilatational and of type *I*. In figure 16(*a*) the maximum integrated growth rate for different *Re* is plotted. Also, in figure 16(*b*, *c*) the wavenumber variation along this maximum growth ridge is plotted as well as f_{max}. The integrated growth rate is plotted as a function of downstream position. An increase in Reynolds number gives a higher maximum growth rate and a shift of the maximum downstream. At the lowest Reynolds number there is a small growth, which can barely be seen in the graph. The wavenumber is plotted against x/Re. An increased Reynolds number gives an increased wavenumber, i.e. shorter waves. Also, the most amplified frequency is plotted as a function of Reynolds number and the graph shows that an increase in *Re* gives a higher frequency. These results are calculated with the same velocity distribution as in figures 9 and 10.

Figure 17 is the experimental equivalent to figure 16. The six images, (*a*–*f*), are taken from the central part of the jet and represent an increase in *Re* from left to

https://doi.org/10.1017/S0022112003005871 Published online by Cambridge University Press

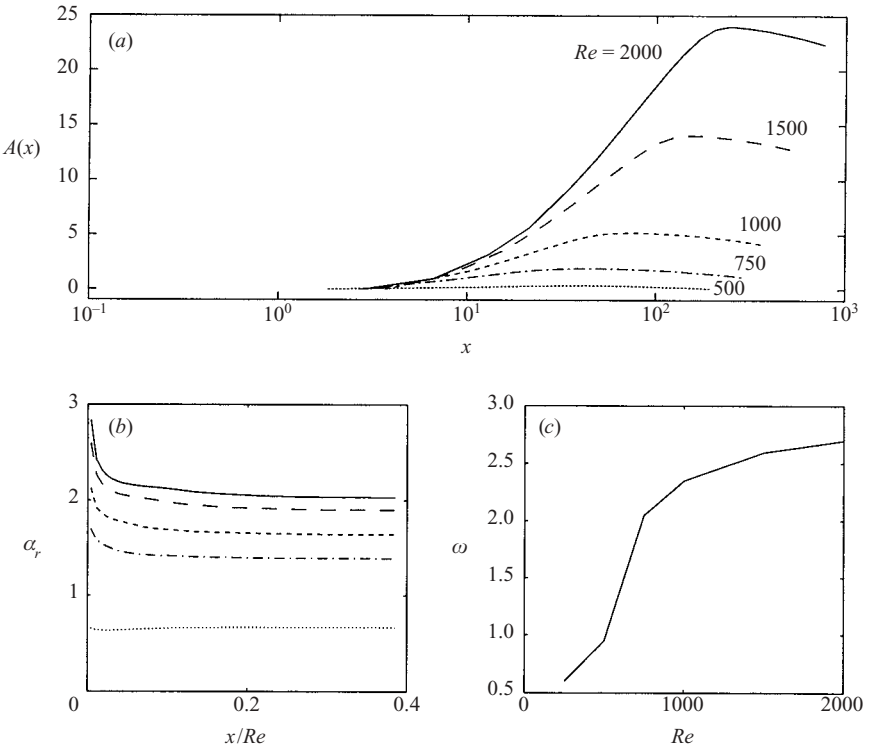


FIGURE 16. Integrated growth for the dilatational mode of type *I*, $Re = 500$, 750, 1000, 1500 and 2000. (*a*) Maximum integrated growth, (*b*) most amplified wavenumber and (*c*) most amplified frequency.

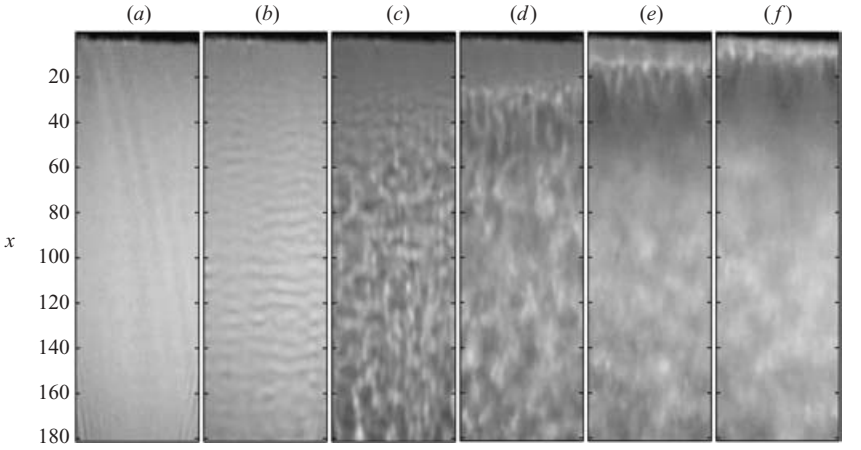


FIGURE 17. Shadowgraph visualization of the breakup of a plane liquid jet. (*a–f*) $Re = 700$, 830, 920, 1050, 1330, 1680 respectively.

right. In figure 17(*a*) $Re = 700$ and no waves can be seen. At the top of the image the nozzle is visible and the downstream position x is shown on the vertical axis. As the velocity (or equivalently Re) increases waves start to appear in the image. These are not forced but naturally occurring, and do not have the same spanwise homogeneity as the forced waves, figure 12(*b*).

https://doi.org/10.1017/S0022112003005871 Published online by Cambridge University Press

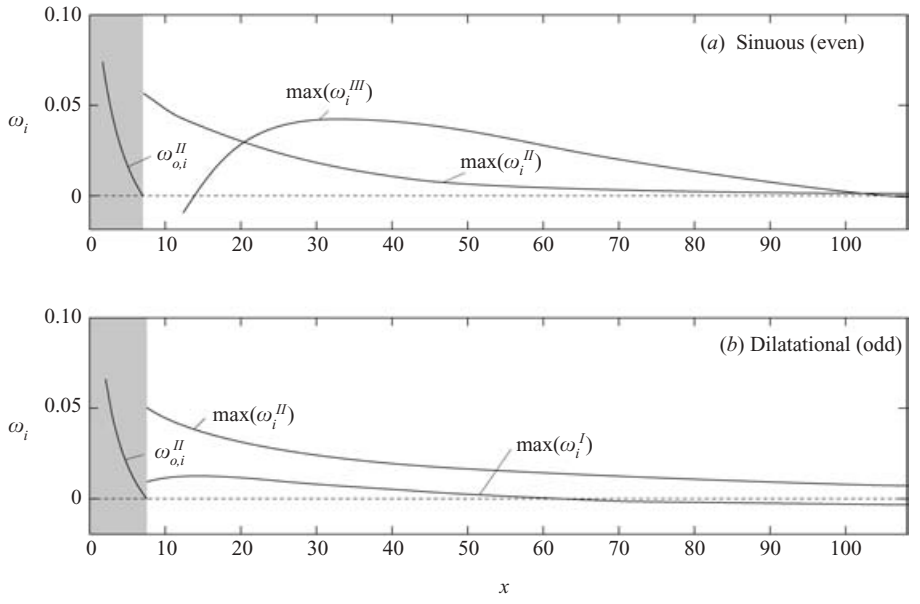


FIGURE 18. Results on the existence of spatial modes in the experimental case presented in figure 12. The grey region indicates absolute instability. In this region $\omega_{0,i}$ is plotted. Also, maximum ω_i for $\alpha_i = 0$ and $\alpha_r = 0 \ldots \infty$ is plotted for the e_{II}, e_{III}, o_I and o_{II} modes.

In figure 17(c) the Reynolds number is slightly higher, $Re = 920$, and the waves break down (jet breakup). The breakdown starts at $x \approx 40$ and is spread in the streamwise direction, i.e. both waves and breakdown can be seen down to $x \approx 100$. When the velocity (Re) is increased even more the breakdown moves upstream, figure 17(d–f). Also, the spanwise extent of the breakdown region seems to shrink.

4.4. *Validity of the comparison with spatial stability calculations*

If the experimental results are to be compared to the spatial stability results the flow cannot be absolutely unstable. If the flow is absolutely unstable the integration contour in the complex ω-plane cannot be lowered to the real axis without encountering a pinch point, hence spatial convective modes cannot exist. In figure 18 calculations for absolute instability for the experimental case, figure 12, are shown. The basic flow field in these calculations, $Re = 700$ in the presence of gravity, is taken from Söderberg & Alfredsson (1998). Figures 18(a) and 18(b) show the results for the sinuous and dilatational modes, respectively. Closest to the nozzle the flow is absolutely unstable, which is indicated with the grey region. In this region the curve $\omega_{0,i}$ is plotted, which corresponds to pinch points. Also, in the graphs the maximum ω_i for $\alpha_i = 0$ and $\alpha_r = 0 \ldots \infty$ can be seen for the e_{II}, e_{III}, o_I and o_{II} modes. These results show that a comparison with spatial stability calculations is valid for $x > 7$.

4.5. *Absolute instability*

The flow was also investigated with respect to absolute instability by searching for pinch points, ω_0, in the complex ω-plane and corresponding saddle points, α_0, in the complex α-plane, see Huerre & Monkewitz (1990). Pinch points were found for the sinuous and dilatational modes of type II but not for the type I modes or for the dilatational type III mode.

https://doi.org/10.1017/S0022112003005871 Published online by Cambridge University Press

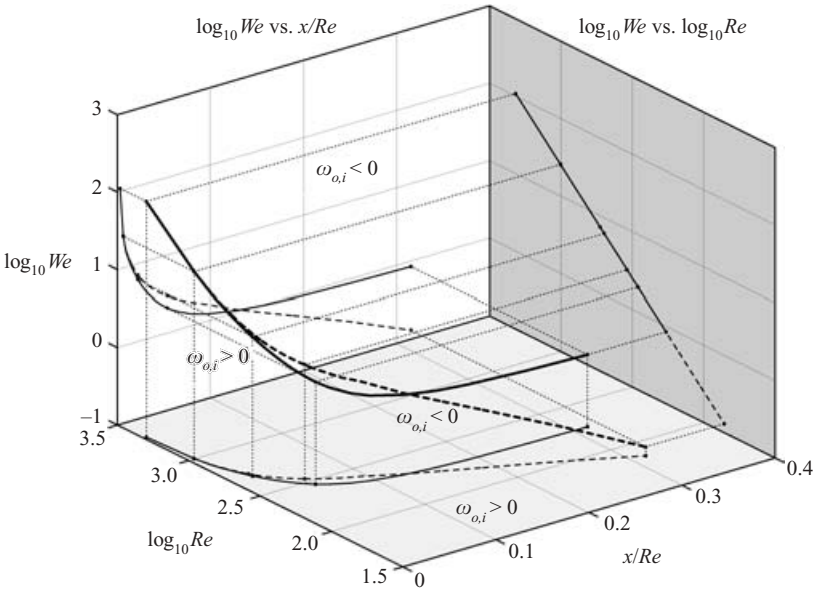


FIGURE 19. The Weber number ($\log_{10} We$) as a function of x/Re and $\log_{10} Re$ for the line $\omega_{0,i} = 0$. —, Sinuous and - - -, dilatational modes of type *II*.

As discussed in § 2.2.4 the full dependence of Re and x/Re on $\omega_{0,i}$ has not been solved for but only the locations of pinch points with zero growth rate, $\omega_{0,i}(Re, x/Re) = 0$. This gives two curves, one for the dilatational mode and one for the sinuous mode, and the locations of these lines are in some sense 'neutral' curves. The calculations show that for $x/Re < 0.095$ the sinuous mode pinches before the dilatational mode when the integration contour is lowered in the ω-plane, i.e. $\omega^s_{0,i} > \omega^d_{0,i}$, where superscripts s and d denotes sinuous and dilatational, respectively. For $x/Re > 0.095$ the situation is the opposite, $\omega^s_{0,i} < \omega^d_{0,i}$. Also, the criteria for an absolute instability are fulfilled for both modes along the two curves. As mentioned previously the whole region $\omega_{0,i} > 0$ has not been solved but isolated points distributed within this region have been explored. For all these points $\omega_{0,i} > 0$, which indicates that the flow could be absolutely unstable within this region.

4.5.1. *We as a function of velocity profile and Re*

Figure 19 shows a three-dimensional representation of the line $\omega_{0,i} = 0$ as a function of x/Re, $\log_{10} Re$ and $\log_{10} We$. Thick solid and dashed lines represent the sinuous and dilatational modes respectively. These are also projected onto three different planes (represented by thin solid and dashed lines on the planes). Thin dotted guiding lines are added to simplify the interpretation of the graph. The planes are referred to as *lower* (x/Re, $\log_{10} Re$), *left* (x/Re, $\log_{10} We$) and *right* ($\log_{10} Re$, $\log_{10} We$) planes. A constant value of x/Re represents a fixed velocity profile. As can be seen in the graph the projection of the line onto the *lower* plane gives rise to two regions, either $\omega_{0,i} > 0$ or $\omega_{0,i} < 0$, where $\omega_{0,i} > 0$ implies an absolutely unstable mode.

For fixed x/Re a specific velocity profile is chosen. From the graph it can be seen that all velocity profiles have a region for low Re where both modes give positive growth rates. Closest to the nozzle both modes seem to coalesce into one line, but from this point to $x/Re = 0.13$ the sinuous mode becomes unstable for lower Reynolds numbers than the dilatational mode. However, for velocity profiles further

https://doi.org/10.1017/S0022112003005871 Published online by Cambridge University Press

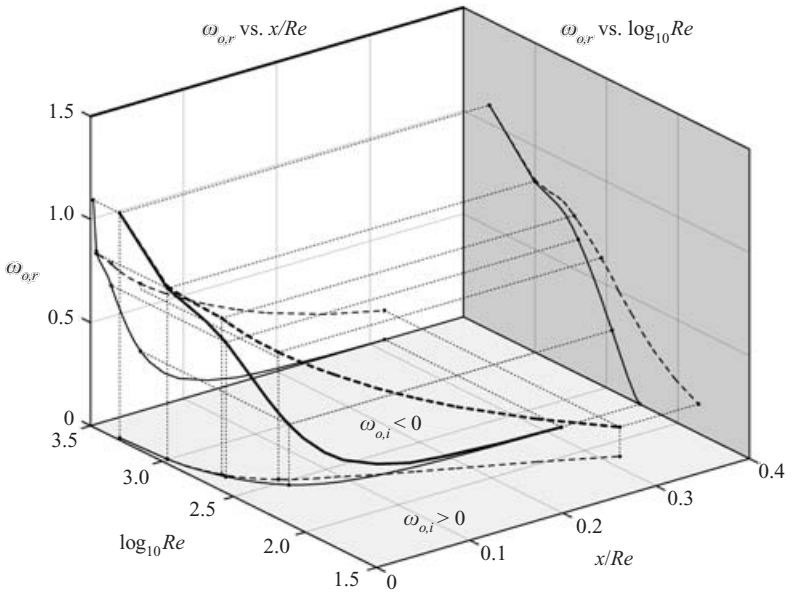


FIGURE 20. The angular frequency ω_r as a function of x/Re and $\log_{10} Re$ for the line $\omega_{0,i} = 0$. —, Sinuous and - - -, dilatational modes of type *II*.

downstream of $x/Re = 0.13$ the situation is the opposite. The downstream behaviour of the two curves is different, where the sinuous mode tends to a constant Reynolds number, $Re \approx 180$, and the dilatational seems to give a linear dependence between $\log_{10} Re$ and x/Re. This indicates that the curve approaches zero Re asymptotically.

Since the Reynolds number is altered by changing the velocity it can be directly related to the Weber number by $We \sim Re^2$. This is clearly seen in the *right* plane, which shows exactly this relation as a straight line given by

$$\log_{10} We = 2 \log_{10} Re + \text{constant}.$$

The *left* plane shows the effect of We, which is similar to the projection onto the lower plane due to the aforementioned relation between Re and We, hence for low We $\omega_{0,i} > 0$. The downstream value of the Weber number tends to $We = 0.83$. This is the global Weber number based on the conditions at the end of the channel (mean velocity in the channel and half channel height). If the Weber number is defined as a local quantity, see table 1, one obtains $\widetilde{We} = 1.0$, which is in agreement with Lin *et al.* (1990). This should be the case since the velocity profile becomes uniform downstream. However, the figure also shows that the dilatational mode can become absolutely unstable at a higher We than the sinuous mode, given a specific profile.

4.5.2. *$\omega_{0,r}$ as a function of velocity profile and Re*

In figure 20 a three-dimensional plot can be seen that has a *lower* plane identical to figure 19 but with the frequency, $\omega_{0,r}$, on the vertical axis. In the *left* plane the frequency dependence of the velocity profile can be seen. The two curves show clear differences between the sinuous and dilatational waves except for the region closest to the channel exit. The dilatational mode has a markedly higher frequency, which steadily decreases along the x/Re-axis from a value $\omega_{0,r} \approx 0.8$ closest to channel exit. The sinuous mode behaves differently and drops rapidly to low frequencies (below 10^{-2}).

https://doi.org/10.1017/S0022112003005871 Published online by Cambridge University Press

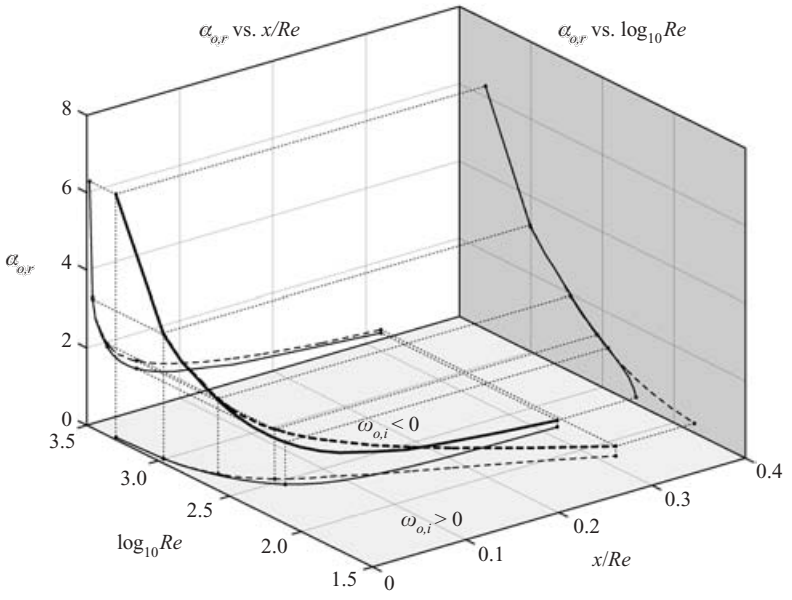


FIGURE 21. The wavenumber α_r as a function of x/Re and $\log_{10} Re$ for the line $\omega_{0,i} = 0$. —, Sinuous and - - -, dilatational modes of type *II*.

The *right* plane show the $\omega_{0,r}$ dependence of *Re*, which is similar to the dependence of position in the jet (it should be kept in mind that the *Re*-axis is plotted in logarithmic scale).

4.5.3. $\alpha_{0,r}$ *as a function of velocity profile and Re*

The last three-dimensional graph, figure 21, shows $\alpha_{0,r}$ as a function of Reynolds number and velocity profile. The curves in the *left* plane clearly show a tendency similar to that of $\omega_{0,r}$ for the decrease in wavenumber (longer waves) and for more uniform velocity profiles (x/Re). Also, the dilatational mode shows a slightly higher wavenumber compared to the sinuous mode. However, a difference with the behaviour of $\omega_{0,r}$ is that the wavenumber variation for the two modes is the same although $\alpha^d_{0,r} > \alpha^s_{0,r}$ throughout the jet except closest to the nozzle where $\alpha^d_{0,r} = \alpha^s_{0,r}$.

The *right* plane of figure 21 shows that the curves fall on top of each other except for the low *Re*. This means that given a specific location in the jet ($x/Re < 0.05$, which is given by the graph) the modes cannot be separated by their wavelength but only by their frequency or as a consequence, their phase speed.

4.5.4. *Local and global We*

Figure 22(*a*) shows the global Weber number variation for the curve $\omega_{0,i} = 0$ as a function of x/Re. This is the same variation as can be found in the *left* plane of figure 19 and is used here for reference. The graph clearly shows that the global Weber number varies over a span of two orders of magnitude. As mentioned in the previous section this gives a result that is in agreement with the theory for a uniform liquid sheet downstream in the jet. However, from knowledge of uniform liquid sheets it is clear that the absolute instability is a direct effect of the surface tension and hence the Weber number. In the region directly after the nozzle the surface velocity is clearly different from the mean velocity of the jet. With this in mind it might be

https://doi.org/10.1017/S0022112003005871 Published online by Cambridge University Press

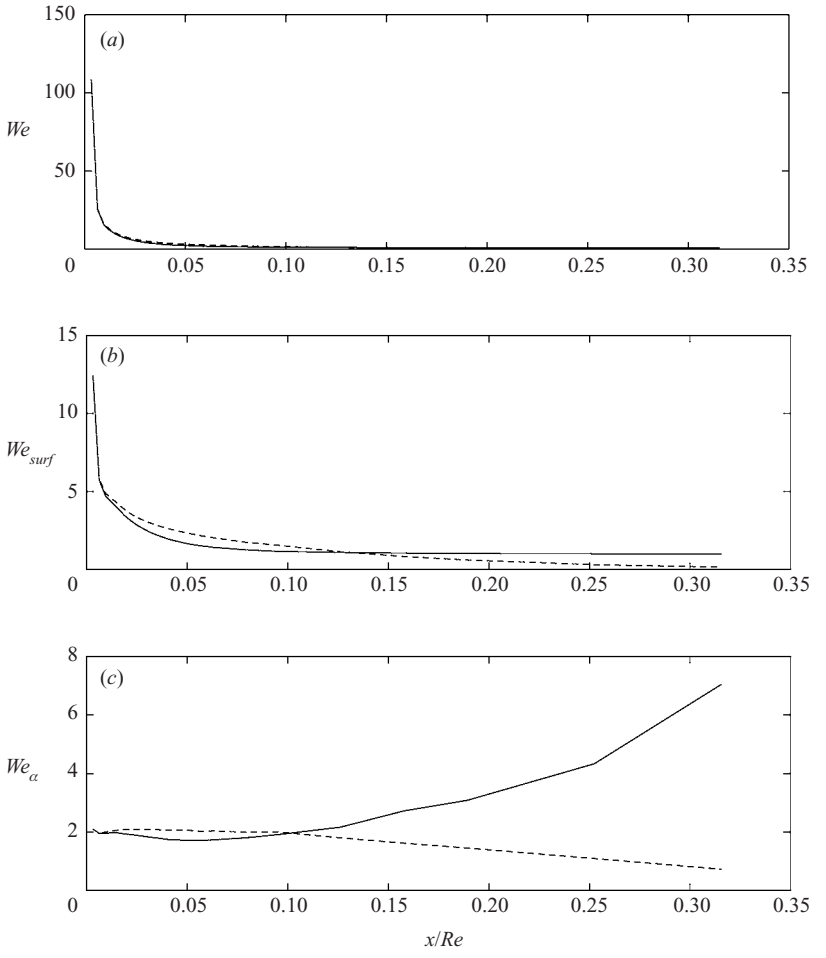


FIGURE 22. Weber number variation for $\omega_{0,i}$: (*a*) *We*, (*b*) We_{surf} and (*c*) $We/\alpha_{0,r}$.

more relevant to look at a surface Weber number defined as

$$We_{surf} = \frac{\rho U_{surf}^2 \tilde{h}}{\gamma},$$

in which U_{surf} is the local surface velocity. This gives a smaller range of *We*. The streamwise position where the curve for the sinuous mode levels out at $We_{surf} = 1$ (within 5% of its final downstream value) is reached at $x/Re = 0.15$ (figure 22*b*). In this region local surface velocity and local jet thickness seem to be the controlling parameters. For the dilatational mode We_{surf} appears to go to zero.

5. Discussion

All results presented are for a plane water jet flowing out into air, and the parameter variation in the experiments is obtained by a change in the jet velocity. Hence, both the Reynolds number and the Weber number change simultaneously. This method of parameter variation has also been used in the stability calculations.

https://doi.org/10.1017/S0022112003005871 Published online by Cambridge University Press

All calculations have been made under the parallel flow assumption; hence the validity is unclear close to the nozzle where the variation in the streamwise velocity profiles is strong. Since the velocity field scales linearly with the Reynolds number, the assumption of parallel flow will be more justified for higher Reynolds numbers. As an example consider the case of a dilatational mode at a position where the velocity profile is almost uniform, e.g. $x/Re = 0.3$, for $\omega_{0,i} = 0$ in figure 20. The Reynolds number at this point is low, $Re \approx 70$, which gives $x \approx 21$. The corresponding wavenumber is $\alpha_r = 0.25$, figure 21, which gives a wavelength $\lambda = 2\pi/\alpha_r \approx 25$. Hence the wavelength is longer than the distance for profile relaxation, which implies that the use of the local parallel flow assumption is questionable for low Reynolds numbers. For the present experiments $Re = 700$–1700, but still the results are questionable closest to the nozzle because of the fast profile relaxation variation in this region, i.e. strong non-parallel effects are present.

In § 4.1 all calculations are performed with a real frequency (wavenumber) for the spatial (temporal) case and the possibility of an absolute instability is not investigated at all. This means, based on the results in § 4.5, that in some regions, which are shown as convectively unstable in figures 9 and 10, the flow is actually absolutely unstable.

Regarding the validity of the comparisons between experiments and numerical results it should be noted that $Re = 700$. From figure 19 it can be seen that this Reynolds number gives a region with absolute instability from $x/Re = 0$ to $x/Re = 0.013$; thus $x \approx 9$. Also, in § 4.4 the experimental case was calculated specifically, and gave the flow as absolutely unstable from the nozzle up to $x \approx 7$. Hence the absolutely unstable region extends less than four channel heights downstream and the question of the validity of the parallel assumption will arise as discussed above. However, from this point and further downstream the flow is only convectively unstable.

5.1. *Spatial convective stability*

The results from the spatial stability analysis show that the wavenumber variation obtained in experiments seems to correspond to modes of type *I*. From the integrated growth rate it appears that the dilatational mode is the most amplified. This is contradictory to the results by Hashimoto & Suzuki (1991). They measured the wave amplitude optically and the results show that the waves are sinuous. Also, they concluded that sinuous disturbances have a higher growth rate than dilatational disturbances. This was based on temporal linear stability calculations where the surrounding gas and Weber number were neglected. However, the linear stability results of Hashimoto & Suzuki (1991) also indicate that surface tension is an important parameter. In their results they show that the surface tension has a stabilizing effect on modes of type *I*. Hence the statement that the sinuous mode is always more amplified than the dilatational may not be general. This can be seen from figure 14, where the integrated growth rate is lower for the sinuous mode than for the dilatational mode.

5.2. *Absolute instability*

The absolute instability is closely connected to the surface tension and for a jet with a uniform velocity profile it has been shown that an absolute instability occurs for sinuous waves when $\widetilde{We} < 1$. For capillary waves on a non-moving fluid the dispersion relation is given by

$$\omega^{*2} = \frac{\gamma \alpha^{*3}}{\rho},$$

https://doi.org/10.1017/S0022112003005871 Published online by Cambridge University Press

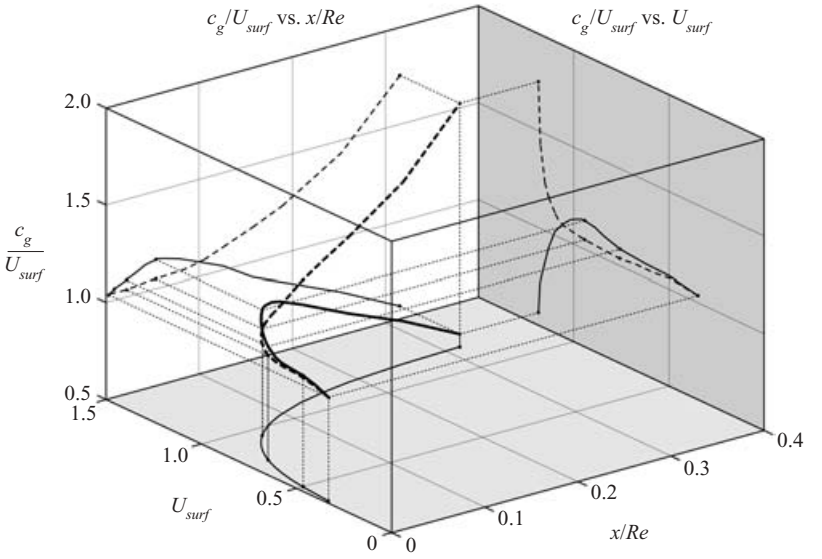


FIGURE 23. Group velocity of capillary waves with a wavenumber given by $\alpha_{0,r}$ for the line $\omega_{0,i} = 0$. —, Sinuous and - - -, dilatational modes of type *II*.

where ω^* is the unscaled angular frequency and α^* the unscaled wavenumber. This gives the phase velocity, c^*, and group velocity, c_g^*, as

$$c^* = \frac{\omega^*}{\alpha^*} = \left(\frac{\gamma\,\alpha^*}{\rho}\right)^{1/2},$$

$$c_g^* = \frac{\mathrm{d}\omega^*}{\mathrm{d}\alpha^*} = \frac{3}{2}\left(\frac{\gamma\,\alpha^*}{\rho}\right)^{1/2}.$$

By non-dimensionalization with a suitable velocity and length scale (U_m and a for this case) these can be expressed as

$$c = \left(\frac{\alpha}{We}\right)^{1/2},$$

$$c_g = \frac{3}{2}\left(\frac{\alpha}{We}\right)^{1/2}.$$

From the results for absolute instability the group velocity for a capillary wave with wavenumber, α_r, can be obtained along the line $\omega_{0,i} = 0$. This is plotted in a three-dimensional graph in figure 23. The lower plane in the graph represents the streamwise position, as in figures 19–21, and the surface velocity u_{surf}. The vertical axis represents the group velocity for a wave with wavenumber α_r, which corresponds to the line $\omega_{0,i} = 0$, scaled with u_{surf} at that position. By examining the projection of the line onto the left plane it is clear that $c_g \approx u_{surf}$ in the region from the channel exit to $x/Re = 0.1$. This is the case for both the dilatational and the sinuous modes. After this region the behaviour is significantly different. The dilatational mode gives an increasing c_g while it decreases for the sinuous mode.

Based on the results on absolute instability it is tempting to generalize the result to two regions in the jet. In the initial phase, when the jet profile experiences a relaxation, the two surfaces of the jet behave independently, which means that the difference

https://doi.org/10.1017/S0022112003005871 Published online by Cambridge University Press

in behaviour for the different symmetries is minor. Far downstream in the jet only the sinuous disturbance shows a pinch point, which gives an absolute instability if $We_{loc} < 1$. This is exactly the result obtained experimentally by Lin & Roberts (1981) and theoretically by Lin *et al.* (1990).

The results obtained regarding an absolute instability for the plane liquid jet should be compared to the cylindrical geometry, where it is a dilatational (varicose) mode that gives absolute instability when the velocity profile is uniform. The reason for this difference is, as mentioned in the introduction, that the surface tension is the driving force of absolute instability for cylindrical jets and for the plane jet it is a stabilizing force. However, the effects that cause absolute instability in the region closest to the nozzle, where the absolutely unstable modes with different symmetry behave in the same way, could also be present in a relaxational cylindrical jet. If the wavelength is short and if the basic flow locally is considered to be plane, i.e. the wavelength is much shorter than the radius of the cylindrical jet, the flow would be similar to that found for the planar case. Hence, this absolutely unstable region could also be present in the cylindrical case. Based on the visualizations performed by Hoyt & Taylor (1977) this could be the case. Their visualizations of a cylindrical relaxational liquid jet showed waves close to the nozzle, which appear to be similar to what is found in the plane geometry. Also, their visualizations show that the waves seem to initiate a breakup similar to that shown in figure 17.

The result by Leib & Goldstein (1986), regarding the absolute instability in a cylindrical jet with velocity profile relaxation does not show the same result as for the plane geometry. This could partly be an effect of the geometry (minimization of surface area/energy, as mentioned in the introduction), but could also be because they used a decaying parabolic velocity profile, i.e. a profile without inflection points. Also, it is possible that they neglected the presence of an ambient gas. It was showed by Lin & Lian (1990) through linear stability analysis that two fundamentally different mechanisms for the breakup of the cylindrical jet can be identified: one is the mechanism that was treated by Rayleigh (1896) where surface tension is the driving force, which breaks the jet up into drops; the second is the interaction between the waves and the ambient air (gas), which creates pressure fluctuations that drive the instability.

5.3. *Frequency selection for naturally occurring waves*

As can be seen in figure 17, the naturally occurring waves are well-defined but do not have the same spanwise homogeneity as the forced waves. This implies either the presence of an external forcing or some frequency selection mechanism. One possibility for this could be the presence of a pocket of absolute instability in the region close to the nozzle. This could serve as a forcing mechanism for the convective modes, which then would be present downstream. From figures 20 and 21 it is possible to see that the frequency and wavenumber for the pinch points lie within the region where the convective modes I are growing.

5.4. *Jet breakup*

The breakup is probably a result of the wave amplitude reaching a level where nonlinear mechanisms initiate the breakup. If one assumes that this takes place for a certain threshold amplitude, the breakup could be explained by figure 16. For low Reynolds numbers the growth reaches a maximum level a certain distance downstream from the nozzle; further downstream it decays. If this maximum is below the threshold amplitude only waves will be seen on the jet. As the Reynolds number increases the maximum integrated growth rate will also increase and move

https://doi.org/10.1017/S0022112003005871 Published online by Cambridge University Press

downstream. If the maximum amplitude is close to the threshold, breakup will appear randomly (*cf.* boundary-layer transition). An increase of the Reynolds number will also move position where the threshold limit is reached upstream, i.e. the breakup moves upstream toward the nozzle.

As an example one could consider the case $Re = 750$ in figure 16 and assume that this corresponds to an amplitude which is slightly below the threshold level. When the Reynolds number is increased to $Re = 1000$ the threshold level is reached and the breakup is clearly visible at a distance downstream of the channel exit (*cf.* figure 17). If the Reynolds number is increased further the threshold amplitude will be reached at a position closer to the nozzle, see figure 16. Also, the growth rate is increasing at this position, which gives a narrower (in the streamwise direction) breakup region. This hypothesis assumes that the initial amplitude at the channel exit is constant.

6. Conclusions

A plane liquid jet shows the presence of wave disturbances. These give rise to waves on the jet surface, which can be visualized by the shadowgraph method. At higher Reynolds number these waves seem to initiate a jet breakup. This breakup moves upstream toward the channel nozzle with increasing Reynolds number.

Local linear stability analysis shows that the relaxational liquid jet has five modes that can become unstable, three sinuous and two dilatational. Results obtained with the spatial linear stability formulation show good agreement with experimental results regarding the wavenumber variation of the waves. The wavenumber can be extracted with good accuracy from shadowgraph visualizations of the plane jet by a continuous Morlet-wavelet transform. Also, this gives the amplitude variation of the waves, which together with the theoretical integrated growth seem to indicate that the observed waves are due to a dilatational disturbance.

The relaxational plane liquid jet has a pocket of absolute instability for one sinuous and one dilatational mode. This is in contrast to the case of a jet with uniform velocity profile, where only the sinuous mode can be absolutely unstable. However, far downstream in the relaxational plane liquid jet the sinuous mode is the only absolutely unstable mode.

The frequency selection for the observed waves is believed to be related to the region of absolute instability located close to the channel exit. This could serve as a forcing mechanism for the convectively unstable disturbances.

REFERENCES

Farge, M. 1992 Wavelet transforms and their applications to turbulence. *Annu. Rev. Fluid Mech.* **24**, 395–457.

Hagerty, W. W. & Shea, J. F. 1955 A study of the stability of plane fluid sheets. *J. Appl. Mech.* **22**, 509–514.

Hashimoto, H. & Suzuki, T. 1991 Experimental and theoretical study of fine interfacial waves on thin liquid sheet. *JSME Intl J.* **34**, 277–283.

Hoyt, J. W. & Taylor, J. J. 1977 Waves on water jets. *J. Fluid Mech.* **83**, 119–227.

Huerre, P. & Monkewitz, P. A. 1990 Local and global instabilities in spatially developing flows. *Annu. Rev. Fluid Mech.* **22**, 473–537.

Leib, S. J. & Goldstein, M. E. 1986 The generation of capillary instabilities in a liquid jet. *J. Fluid Mech.* **168**, 479–500.

Li, X. & Tankin, R. R. 1991 On the temporal stability of a two-dimensional viscous liquid sheet. *J. Fluid Mech.* **226**, 425–443.

https://doi.org/10.1017/S0022112003005871 Published online by Cambridge University Press

Lienhard, J. H. 1968 Effects of gravity and surface tension upon liquid jets leaving Poiseuille tubes. *Trans. ASME*: *J. Basic Engng* **226**, 425–443.

Lin, S. P. & Lian, Z. W. 1990 Mechanisms of the breakup of liquid jets. *AIAA J.* **28**, 120–126.

Lin, S. P., Lian, Z. W. & Creighton, B. J. 1990 Absolute and convective instability of a liquid sheet. *J. Fluid Mech.* **220**, 673–689.

Lin, S. P. & Roberts, G. 1981 Waves in a viscous liquid curtain. *J. Fluid Mech.* **112**, 443–458.

de Luca, L. 1999 Experimental investigation of the global instability of plane sheet flows. *J. Fluid Mech.* **399**, 355–376.

de Luca, L. & Costa, M. 1997 Instability of a spatially developing sheet. *J. Fluid Mech.* **331**, 127–144.

Plateau, J. 1873 *Statique Expérimentale et Théorique des Liquides Soumis aux Seules Forces Moléculaires*. Cited in Rayleigh (1896).

Rayleigh, Lord 1896 *Theory of Sound*, 2nd edn. Dover.

Savart, F. 1833 *Ann. Chem.* **53**, 337.

Schlichting, H. 1979 *Boundary Layer Theory*, 7th edn. McGraw-Hill.

Söderberg, L. D. & Alfredsson, P. H. 1998 Experimental and theoretical stability investigations of plane liquid jets. *Eur. J. Mech.* B/*Fluids* **17**, 689–737.

Squire, H. B. 1953 Investigation of the instability of a moving liquid film. *Br. J. Appl. Phys.* **4**, 167–169.

Tillet, J. P. 1968 On the laminar flow in a free jet of liquid at high Reynolds numbers. *J. Fluid Mech.* **32**, 273–292.

https://doi.org/10.1017/S0022112003005871 Published online by Cambridge University Press